THE OHIO STATE UNIVERSITY

AERONAUTICAL AND ASTRONAUTICAL ENGINEERING 515-H

ADVANCED HYPERSONIC AIRCRAFT DESIGN

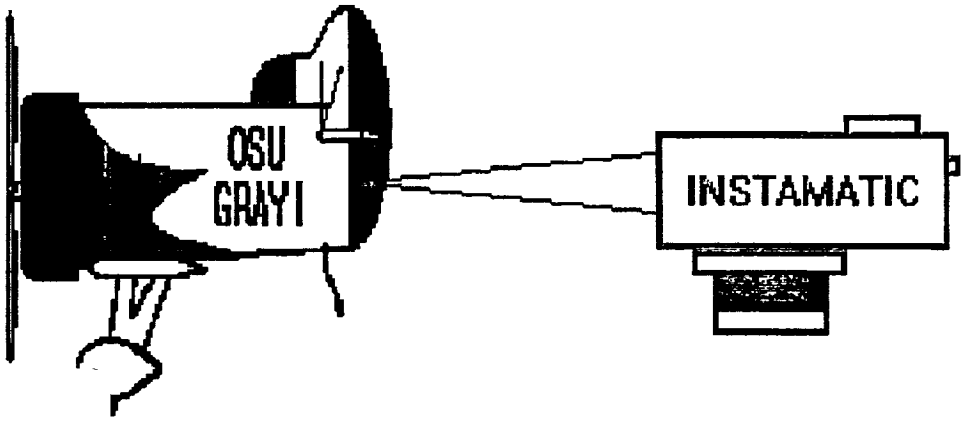

June 1, 1992

Group Leader: Rob Utzinger

Hans-Joachim Blank

Craig Cox

Greg Harvey

Mike McKee

Dave Molnar

Greg Nagy

Steve Petersen

ACKNOWLEDGMENTS

Dr. G. Gregorek, The Ohio State University

Dr. J. Haritonidis, The Ohio State University

Dr. R. Edse, The Ohio State University

General Electric Aircraft Engines

NASA Lewis Research Center

Ray, Civil/Aero Shop

Bob Leiweke

TABLE OF CONTENTS

LIST OF FIGURES

LIST OF TABLES

INTRODUCTION

As a result of the recent Persian Gulf conflict, a need for more imagery collection systems for tactical reconnaissance has become apparent. The Air Force RF-4Cs, Navy F-14s, and Army, Navy, and Marine unmanned aerial vehicles each operated within the limitations of their designs, and with the retirement of the SR-71, the military lacks a reconnaissance vehicle with real-time, broad-area, all-weather, and night capabilities with an extended range. The objective of this design project is to develop the hypersonic reconnaissance aircraft that is sorely needed to replace the SR-71 and to complement existing intelligence gathering devices.

The initial design considerations were to create a manned vehicle which could complete its mission with at least two airborne refuelings. The aircraft must travel between Mach 4 and Mach 7 at an altitude of 80,000 feet for a maximum range of 12,000 nautical miles. The vehicle should have an air breathing propulsion system at cruise. With a crew of two, the aircraft was designed to carry a payload of 7500 lbs. within 250 cubic feet. The plane should be able to take off and land on a 10,000 foot runway, and the yearly operational costs were not to exceed $300 million. Finally, the aircraft should exhibit stealth characteristics, including a minimized radar cross-section (RCS) and a reduced sonic boom. The technology used in this vehicle should allow for production between the years 1993 and 1995.

The aircraft was intended to complement the tanker aircraft concurrently designed by "Top Gun Team", Ecole Polytechnique Institute, France.

CONFIGURATION HISTORY

In the initial phases of the development of our design concept, our major concern was to keep the refueling points at a reasonable distance from the target for the 12,000 nautical mile mission. Therefore, we decided that a maximum non-refueled cruise range of 5,000 nautical miles would provide a safe refueling point for the vehicle. Another design consideration was to keep the operating cost below $300 million per year. This is a major concern since the SR-71 cruised at much lower speeds but required the same amount of funds to operate as our vehicle must.

We initially examined two configurations: a waverider and a conventional design. The waverider appeared advantageous due to its high cruise efficiency. We surmised that this would allow us to build a lighter aircraft than the conventional design would. Instead, the waverider did not provide enough volume to store all the necessary liquid hydrogen (LH2) fuel. When methane was considered, we determined that the aircraft would weigh more than 40% greater than a LH2 fueled conventional design. Therefore, the volumetrically inefficient waverider was ruled out as a possibility.

By conducting a trade study, it was determined that by reducing the take-off weight and later refueling to the maximum capacity 3,500 nautical miles down range, the total fuel burned during the first leg of the mission could be reduced and, more importantly, the total refueling time could be cut considerably.

Three integrated turbo-ramjets were necessary to power the aircraft for this mission. The initial design utilized four over-under turbo-ramjets. A large amount of excess thrust below Mach 1 and at low Mach numbers suggested that we should remove an engine. We switched to the integrated turbo-ramjet because it would weigh about 15 % less, cause less drag since the engine box would be smaller, and allow easier access to the turbojets for maintenance. In order to simplify the

refueling process and the fuel system complexity, both the turbojets and the ramjets were designed to burn hydrogen.

At the cruise environment of Mach 5 at 80,000 feet, high skin temperatures were expected. To deal with the extreme temperatures encountered, nickel superalloys were proposed for the leading edges of the wings and the nose, while carbon-carbon composite materials would be suitable for the exit nozzle. No active cooling was presented except within the engine box. The cryogenic tank systems would utilize flushing the insulation with an inert gas to prevent excessive boil-off of fuel.

For the aerodynamic study, a flat plate delta wing configuration was used to calculate lift and drag for the entire flight envelope. A double delta planform was selected so that the strake would have a subsonic leading edge, decreasing wave drag. The main wing has a supersonic leading edge at cruise. Both portions of the wing employ a 5% thick symmetrical double wedge airfoil because this proved to be the best compromise between aerodynamic efficiency and ease of manufacturing.

Figure 1 details the proposed configuration, and Table 1 shows the basic specifications of the aircraft.

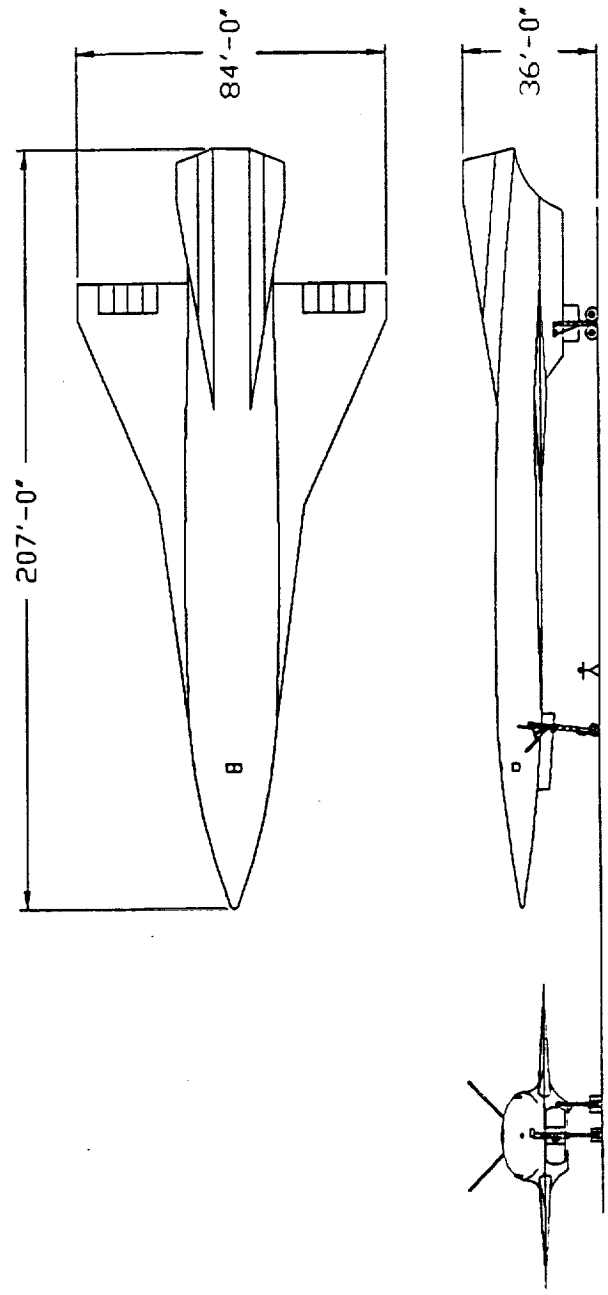

Figure 1: Three View

Table 1: Specifications

Configuration	Conventional Double Delta
Length	207 ft.
Span	84 ft.
Height	36 ft.
Engines	3 LH2 Integrated Turbo-Ramjets
Maximum Gross Weight	281,000 lbs.
Planform Area	3000 sq.ft.
Aspect Ratio	2.4
Strake Leading Edge Sweep	82.5 deg.
Main Wing Leading Edge Sweep	66.5 deg.
Airfoil	5% Symmetric Double Wedge
Cruise Speed	Mach 5.0
Cruise Altitude (5000 nm. Climbing Cruise)	80,000 - 105,000 ft.
Maximum Speed	Mach 5.6 at 112,000 ft.
Service Ceiling	112,000 ft
Take Off Distance (Max Gross Weight)	8,600 ft.
Landing Distance (85% Max Gross Weight)	5,800 ft.
Take Off Speed	136 kts.
Maximum Range, No Refueling	7,400 nm.

WEIGHT ANALYSIS

The initial sizing of the aircraft was based on a carpet plot and research of hypersonic vehicles. The carpet plot can be seen in Figure 2. Assuming an aspect ratio of 2.0 and a wing area of 3,000 ft^2, the governing parameters are the climb, 2g maneuvering curve, and the 120 knot stall speed in the landing configuration. From research the average wing loading for hypersonic vehicles was found to be 80. Using this information, the initial estimated take-off weight of the aircraft was 240,000 pounds.

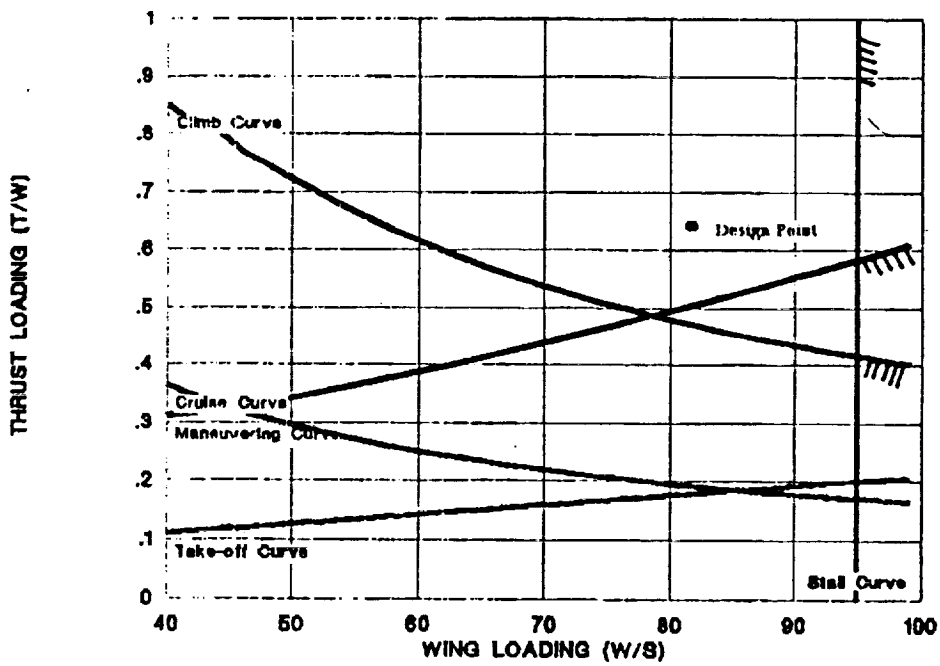

Figure 2: Carpet Plot

After an estimate of the take-off weight was found, the weight was validated using the output of the WAATS program. Since the WAATS program is designed for hypersonic transport aircraft, it required some modification for military

reconnaissance aircraft application. From WAATS, the dry weight was determined to be 128,100 pounds and the maximum gross weight was 290,000 pounds. However, the take-off weight was based on a maximum cruise range of 6,000 nautical miles with reserves. Since the take-off weight would be modified to accommodate a refueling at 3,500 nautical miles down range, the maximum gross weight appeared to be reasonable.

During the initial sizing for take-off, a trajectory starting at maximum gross weight and a trajectory starting with the necessary fuel to reach the first refueling point were examined. The analysis was performed by stepping the aircraft through an accelerated climb, constant speed cruise climb, power on descent, and constant speed refueling using part of a program written by Bob Leiweke, Yan Akerjordet, and Dave Sujudi. During each increment of the trajectory the time, distance, altitude, and amount of fuel burnt was calculated. It was found that take-off at maximum gross weight minimized the refueling time, but required more fuel during the ascent and cruise because of the additional weight. It was also found that take-off with the necessary fuel to reach the first refueling point required less fuel during the ascent and cruise, but drastically increased the refueling time. The weight which optimized both considerations at take-off was a weight of 245,000 pounds.

During the trajectory analysis the maximum gross weight of the aircraft was iterated to accommodate a 6,000 nautical mile cruise with reserves. From this iteration process, the final maximum gross weight of the aircraft was 281,000 pounds. As a summary, the weight distribution chart is shown in Figure 3. The weight distribution table can be seen in Table 2.

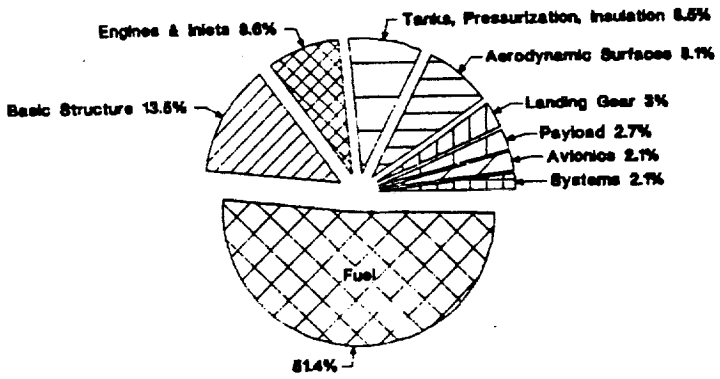

Figure 3: Weight Pie Chart

Table 2: Aircraft Weight Distribution

SYSTEM	WEIGHT	
Body Structure:		42,000 lbs.
Basic	38,500 lbs.	
Secondary	3,000 lbs.	
Thrust	500 lbs.	
Aerodynamic Surfaces:		23,000 lbs.
Wing	15,000 lbs.	
Vertical Tails	8,000 lbs.	
Engines:		18,000 lbs.
Landing Gear:		8,500 lbs.
Systems:		12,600 lbs.
Fuel	1,000 lbs.	
Control	2,000 lbs.	
Inlet	1,000 lbs.	
Electrical	2,000 lbs.	
Crew	1,000 lbs.	
Avionics	5,600 lbs.	
Tanks:		24,000 lbs.
Fuel Tanks	10,000 lbs.	
Insulation	3,000 lbs.	
Pressurization	11,000 lbs.	
TOTAL:		128,100 lbs.
Payload	7,500 lbs.	
Crew	400 lbs.	
LH_2 Fuel	145,000 lbs.	
MAXIMUM GROSS WEIGHT:		281,000 lbs.

TRAJECTORY ANALYSIS

The operating envelope for our aircraft defines the operating limitations such as the maximum dynamic pressure, aerodynamic heating, stall speed, and engine limitations as a function of Mach number and altitude. The operating envelope for our aircraft can be seen in Figure 4.

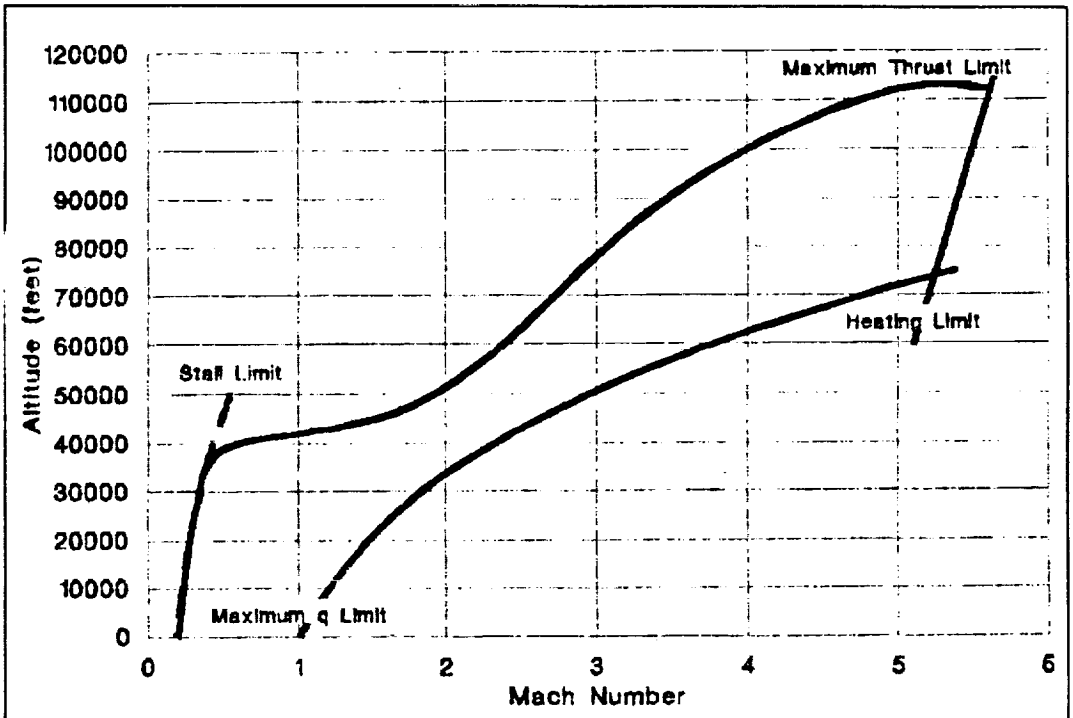

Figure 4: Operating Envelope

The maximum thrust limit contour is the zero specific excess power contour. The specific excess power represents the aircraft's ability to climb and or accelerate, at any altitude and Mach number. If the specific excess power is equal to zero, the aircraft is flying level, decelerating while climbing, or accelerating while descending [Daniel P. Raymer, pg. 472]. The contour shows that the aircraft has the capability to operate in level flight at Mach 5.0 between 80,000 feet and 105,000 feet for a cruise climb. The aircraft can also perform its refueling requirement of Mach 0.8 at

40,000 feet. The envelope also shows that the maximum service ceiling is approximately 112,000 feet at maximum speed of Mach 5.6. The lower limit of the operating envelope is the Q-limit or maximum dynamic pressure limit of the aircraft which is 1500 lb/ft^2. The Q-limit is the structural limitation of the aircraft.

Finally, the aerodynamic heating limit is the maximum skin temperature limit of the aircraft due to thermal energy transferred to the aircraft by convection [Leland M. Nicolai, pp. 4-1 - 4-6].

To examine the trajectory path of the aircraft from take-off, two programs written by Bob Leiweke, Yan Akerjordet, and Dave Sujudi were modified and used. The two trajectories examined were the minimum time-to-climb trajectory and the minimum fuel-to-climb trajectory. The minimum time-to-climb curves are the specific excess power curves. Specific excess power is defined as the change in specific energy with respect to change in altitude [Daniel P. Raymer, p. 472].

$$P_S = V[(T/W)-(qC_{D_O}/(W/S))-n^2(K/q)(W/S)]$$

The minimum fuel-to-climb curves are developed from the specific fuel consumption curves. Specific fuel consumption is defined as the change in specific energy with respect to change in fuel weight [Daniel P. Raymer, pg. 478].

$$F_S = P_S/(SFC\ T)$$

The contour plots can be seen in Figures 5 and 6. These plots show the altitude versus Mach number path that should be followed to minimize the time-to-climb and fuel-to-climb. The aircraft follows a constant-Q trajectory where it intercepts a constant-Q of 1000 lb/ft^2.

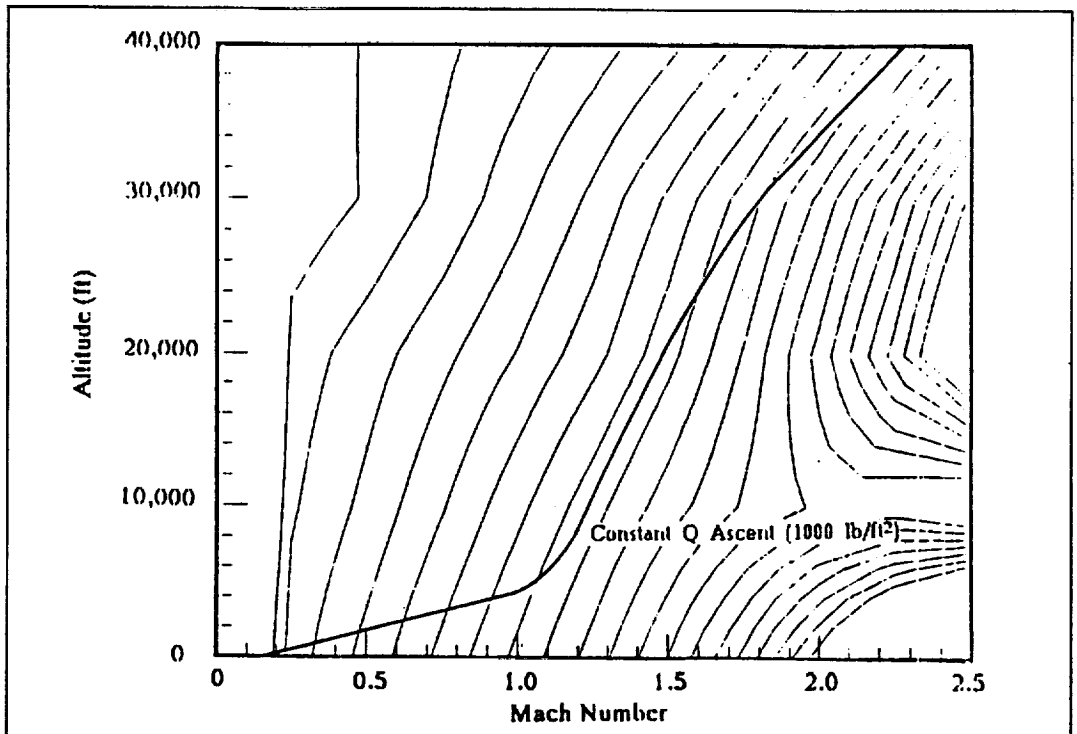

Figure 5: Minimum Time-to-Climb Trajectory

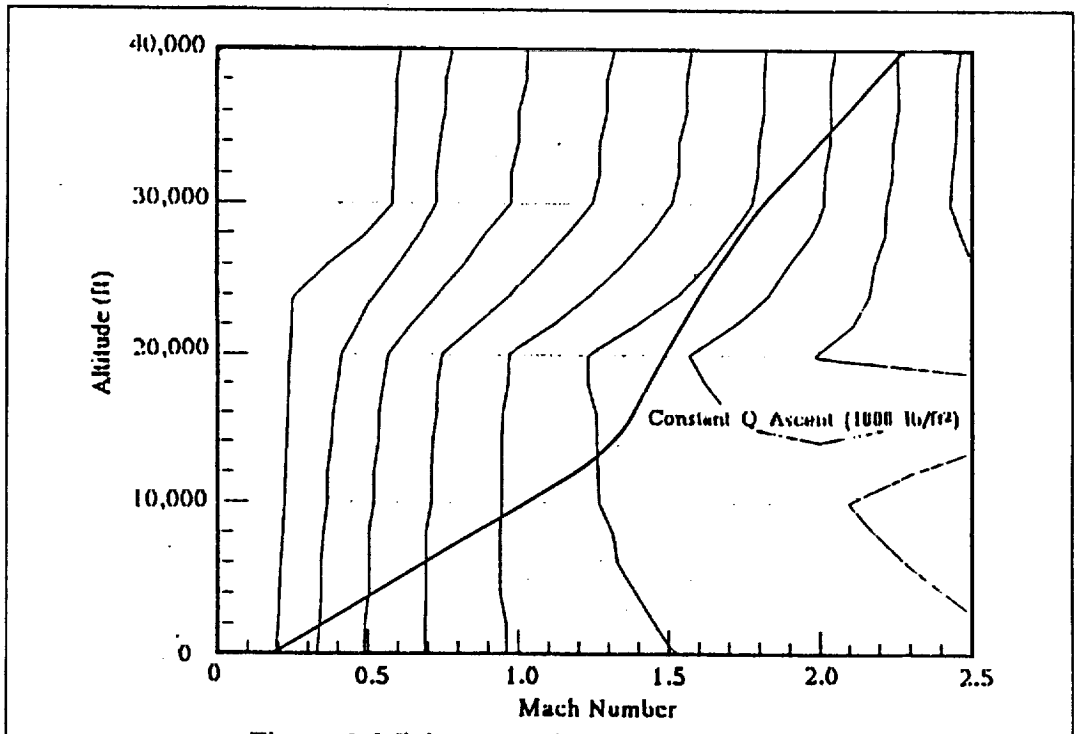

Figure 6: Minimum Fuel-to-Climb Trajectory

To determine the actual trajectory paths, lines of constant energy height were overlaid on the contour plots. Constant energy height lines are based on the equation,

$$h_e = h + V^2/(2g)$$

where h_e = energy height; h = actual height (altitude)

The energy height curves represent the height the aircraft could achieve if all of its kinetic energy is converted to potential energy. The minimum time-to-climb trajectory and minimum fuel-to-climb trajectory are determined by the point at which the energy height curves are tangent to the P_S curves [Daniel P. Raymer, pp. 475-476].

From this analysis, it was determined that there was a 3% fuel savings using the minimum fuel-to-climb trajectory. However, the time savings of the minimum time-to-climb showed that there was less than a 1% time savings. Therefore, the minimum fuel-to-climb trajectory was used for our aircraft. The angle-of-climb and rate-of-climb for the initial ascent are shown in Figures 7 and 8, respectively.

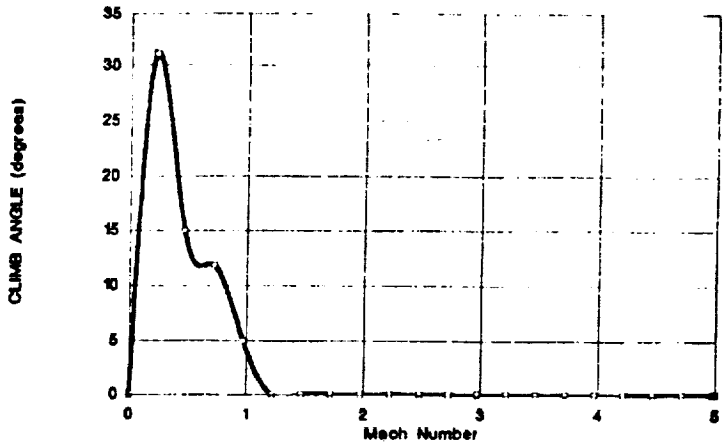

Figure 7: Climb Angle Versus Mach Number

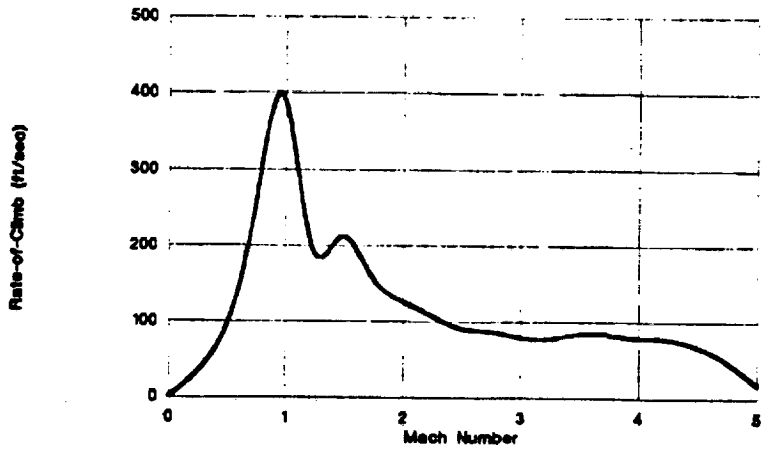

Figure 8: Rate of Climb Versus Mach Number

Using the minimum fuel-to-climb trajectory, an altitude versus distance plot seen in Figure 9 shows the overall mission trajectory of our aircraft. It includes a 3,500 nautical mile cruise to refueling point 1; a 5,000 nautical mile cruise to refueling point 2; and a final cruise of 3,500 nautical miles to land. During each segment of the cruise, the aircraft performs a cruise climb beginning at 80,000 feet and ending at an average altitude of 105,000 feet. The aircraft cruise climbs at a constant L/D of 3.3. The average climb angle for this cruise is approximately 0.75°. The total mission time for the aircraft is approximately 5.3 hours. The time breakdown for the entire mission is shown in Figure 10.

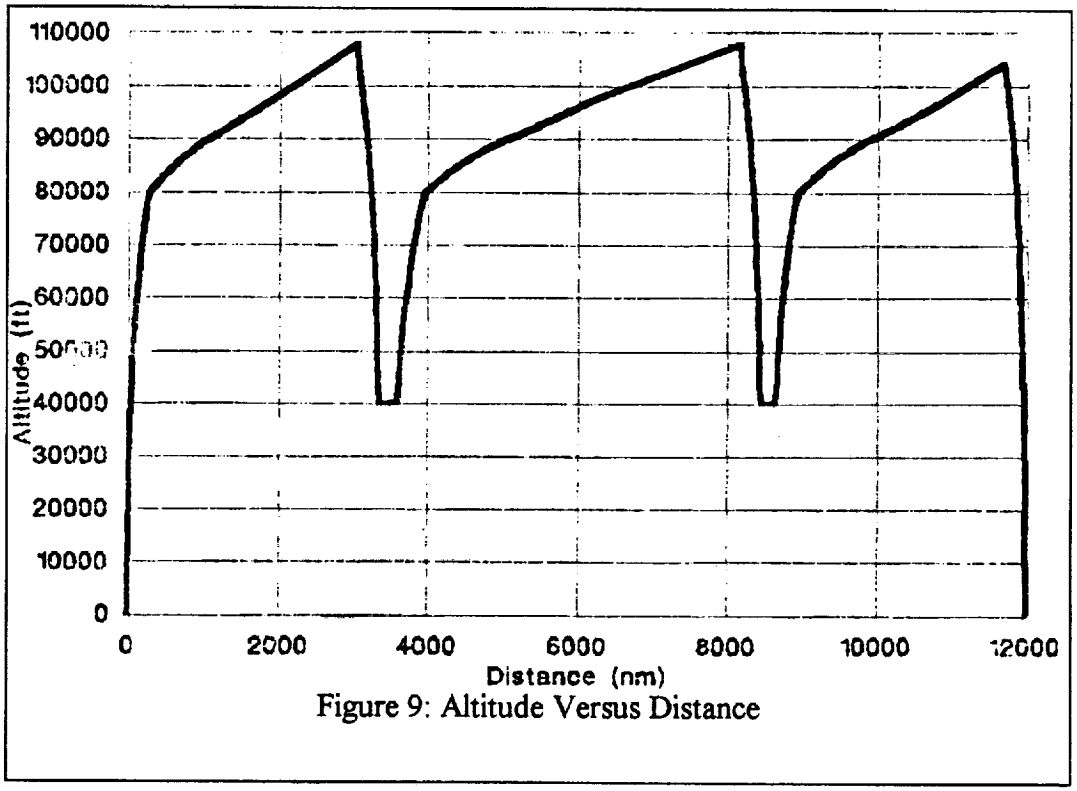

Figure 9: Altitude Versus Distance

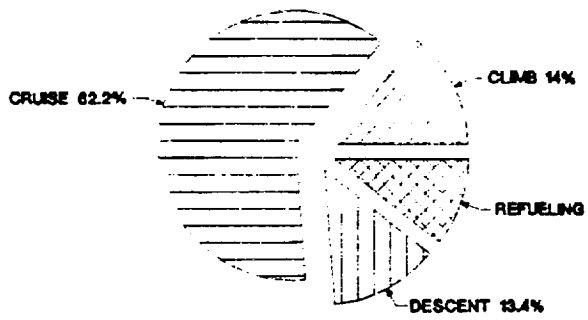

Figure 10: Mission Time Distribution Chart

In order to give an overview of the type of mission which could be performed by our aircraft, Figure 11 gives a perspective of the capabilities of our aircraft. The aircraft could leave from a Hawaiian air base, fly 3,500 nautical miles, and hook-up with a tanker stationed in Guam. The aircraft could then fly a 5,000 nautical mile reconnaissance mission over Vietnam, China, and North Korea. This would require several 2g turns with approximately a 100 nautical mile turn radius. Finally, the aircraft would hook-up again with the tanker at refueling point 2, fly another 3,500 nautical mile cruise, and return to Hawaii.

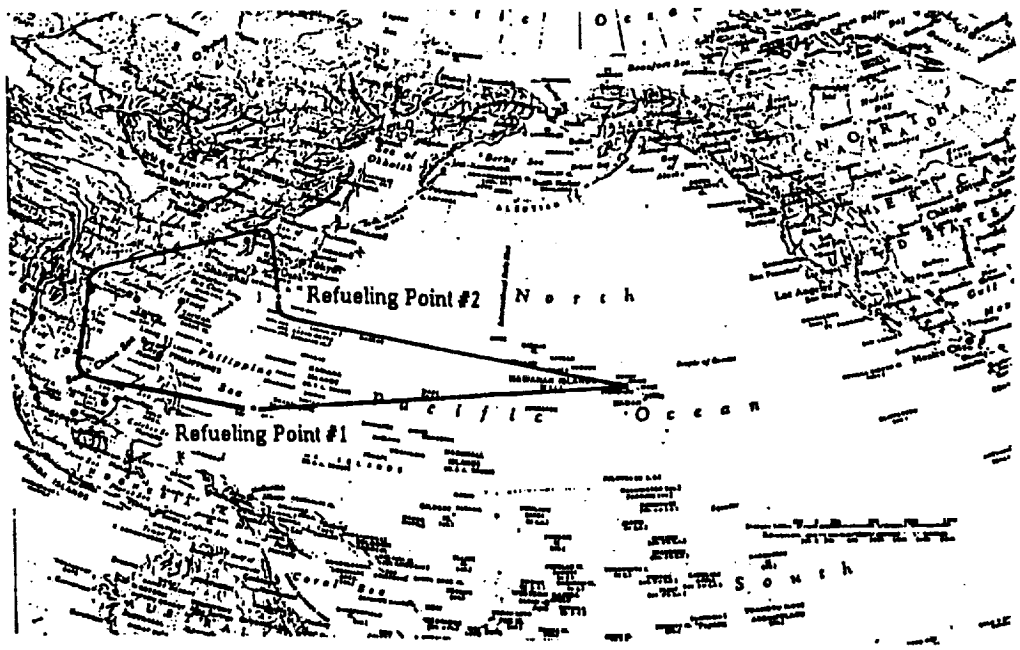

Figure 11: Mission Profile

In addition to the required mission, the trajectory program was run from a maximum gross weight take-off to determine the maximum range of the aircraft with no reserves. The altitude versus distance plot is shown in Figure 12. The maximum range of the aircraft is 7,400 nautical miles with a total mission time of 3 hours.

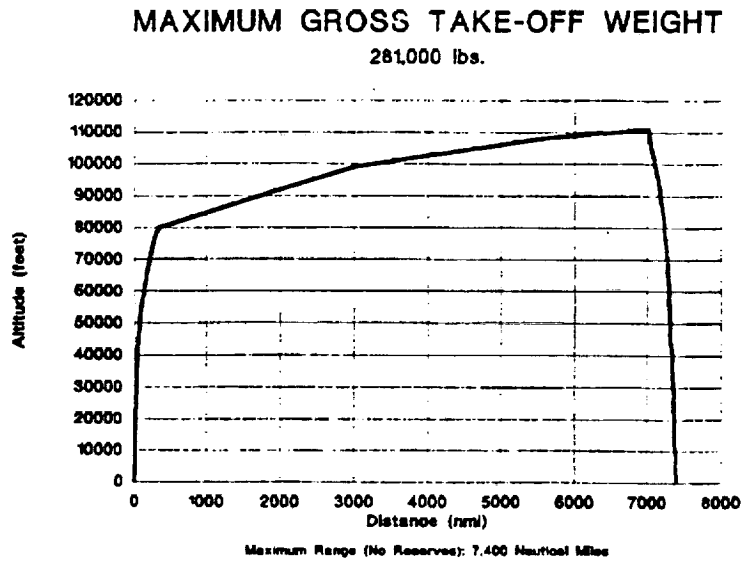

Figure 12: Maximum Range Cruise (No Reserves)

TAKE-OFF & LANDING ANALYSIS

The take-off analysis shown in Figure 13 was conducted using an approximate flap deflection of 25° (C_{Lmax} = 1.43) at a maximum gross weight of 281,000 pounds. The ground roll of the aircraft covers 4,600 feet. The rotation roll, which was approximated by three times the take-off velocity, was 725 feet. This accounted for a total ground roll of 5,325 feet. At take-off, the aircraft is traveling at 136 knots. During the transition to climb, the aircraft travels 625 feet, to an altitude of 22 feet, at an average velocity of 142 knots. After the transition to climb, the aircraft continues its climb to clear a 50 foot obstacle traveling another 400 feet down range. The total take-off distance for our aircraft was 6,350 feet. The total take-off distance is within our 10,000 foot requirement [Daniel P. Raymer, pp. 481 - 484].

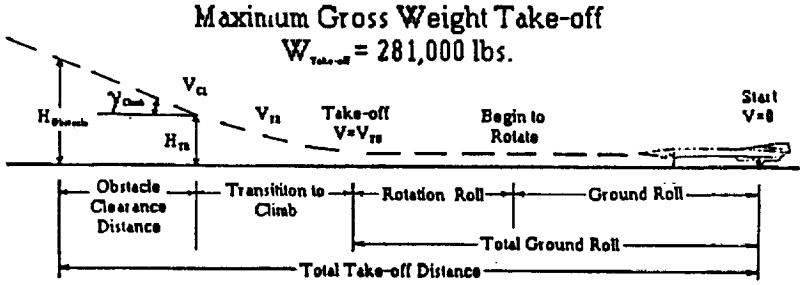

Given Conditions: Take-off With Flaps

Ground Roll Distance = 4,600 feet	Take-off Speed = 136 knots
Rotation Roll Distance = 725 feet	Transition to Climb Speed = 142 knots
Transition to Climb Distance = 625 feet	Initial Climb Speed = 148 knots
Transition Height = 22 feet	Initial Climb Angle = 4°
Obstacle Clearance Distance = 400 feet	Obstacle Clearance Height = 50 feet

Total Take-off Distance = 6,350 feet

Figure 13: Take-off Analysis

The landing analysis shown in Figure 14 was conducted using a flap deflection of approximately 40° (C_{Lmax} = 1.83) at a landing weight of 240,000 pounds or 85% of the maximum gross weight of the aircraft. The aircraft begins its approach at 136 knots with an approach angle of 3°. After clearing a 50 foot obstacle the aircraft travels 770 feet before beginning to flare. The flare begins 10 feet above the runway and the aircraft travels 400 feet before touch down at 125 knots. The aircraft will then free roll 630 feet or the equivalent of a three second delay time at touch down speed. Finally, the aircraft will come to rest after a braking distance of 4,000 feet. The total landing distance is 5,800 feet. The total landing distance is within our 10,000 foot requirement [Daniel P. Raymer, pp. 485 - 487].

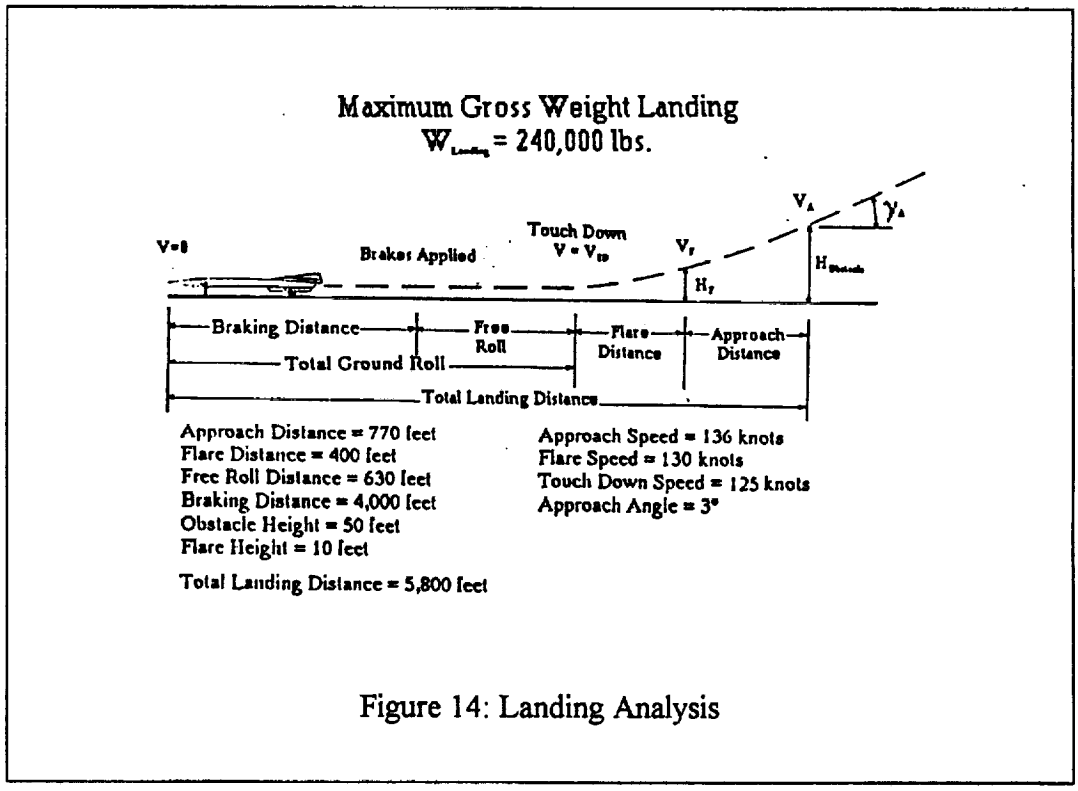

Figure 14: Landing Analysis

The "engine out" take-off analysis shown in Figure 15 is based on a "balanced field length" total take-off analysis. The analysis represents the total take-off

distance required to clear an obstacle in the event an engine fails at the "decision speed". At decision speed the pilot can choose to either take-off or brake to a stop. The analysis was again conducted using an approximate flap deflection of 25° at a maximum gross weight of 281,000 pounds. The total take-off distance to clear a 50 foot obstacle is 9,675 feet. The total stopping distance is 10,125 feet [Daniel P. Raymer, pp. 484 - 485].

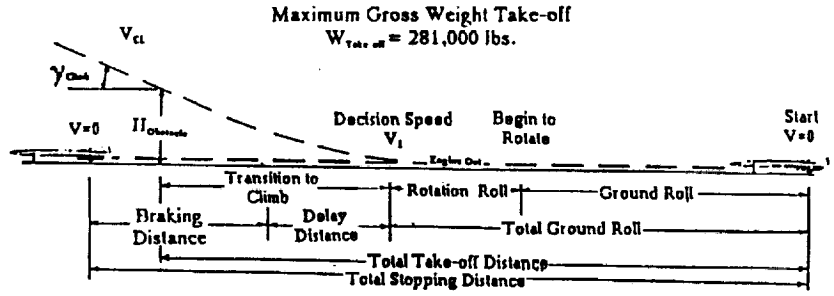

Given Conditions: Take-off With Flaps

Ground Roll Distance = 4,600 feet
Rotation Roll Distance = 725 feet
Transition to Climb Distance = 4,350 feet
Delay Time for Breaking = 200 feet
Braking Distance = 4,600 feet

Total Take-off Distance = 9,675 feet
Total Stopping Distance = 10,125 feet

Take-off Speed = 136 knots
Decision Speed = 142 knots
Climb Speed = 148 knots
Initial Climb Angle = 3.5°
Obstacle Clearance Height = 50 feet

Figure 15: "Engine Out" Analysis

PROPULSION

Engine Analysis

The engines required to power our Mach 5 vehicle created a tremendous challenge. Since the aircraft must operate at a wide variety of speed ranges, a dual engine system was developed. An integrated turbo/ramjet was chosen to facilitate the integration of the propulsion system into the fuselage, to reduce the weight, and to reduce the size of the engine box. Figure 16 shows the engine schematic and the performance characteristics. Three turbo/ramjets are needed to produce the required the thrust for the flight regime. By choosing a dual engine, the aircraft will be able to achieve the wide speed variations with ease.

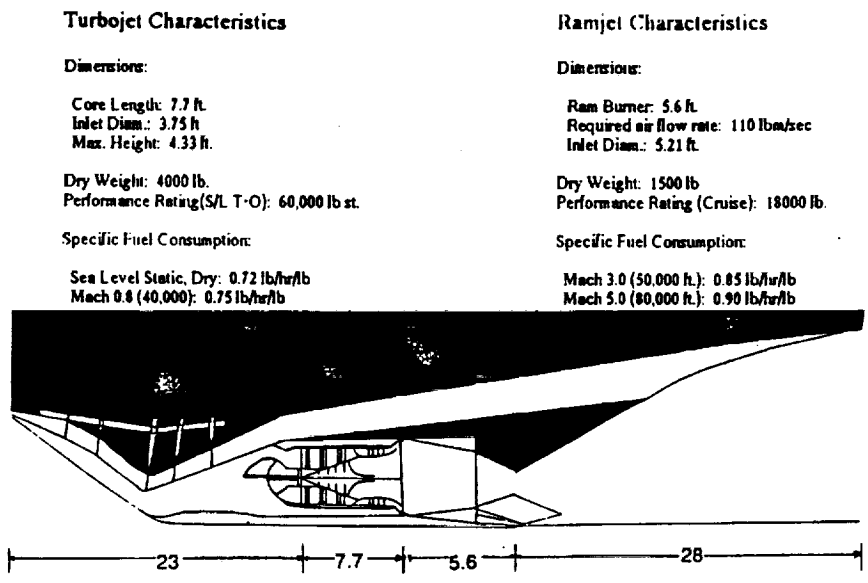

Figure 16: Engine Configuration

Before the integrated turbo/ramjet configuration was selected, numerous dual engine configurations were considered:

Turboramjet:

This configuration consists of a turbojet along with a ramjet. The engines can be integrated either in an over/under, wrap-around, or an in-line configuration. The turbojet is operated up Mach 2.0-3.0 and then the ramjet accelerates the vehicle to Mach 6.0-7.0.

Turbfanramjet:

The configurations are the same as the turboramjet, but the turbofanramjet offers the improved subsonic performance characteristics of the turbofan. The only drawback is the size of the fan relative to the rest of the engine core.

Scramjet:

Scramjets are very efficient in the high speed flight regimes, but do not offer low speed propulsion. They must operate in the Mach 6.0-12.9 region.

The most feasible configuration for our flight conditions was the turbo/ramjet. Even though the turbofanramjet operates more efficiently at lower Mach numbers, the turbojet was chosen to minimize the area taken up by the engine box and to reduce the weight of the engines.

An analysis of the ramjet was first undertaken by analyzing an ideal ramjet. This analysis assumes that the combustion and expansion processes in the engine are reversible and adiabatic, and that the combustion process takes place at constant pressure. These assumptions are not, of course realistic, but it did enable an initial evaluation of the performance of a hydrogen powered ramjet. The ideal ramjet is a

most useful concept, since its performance is the highest that the laws of thermodynamics will permit, and is the limit which real engines will approach if their reversibilities can be reduced.

A typical ramjet engine is shown in the schematic of Figure 17. Using the station numbers of Figure 17, Figure 18 shows a temperature-entropy diagram of the air as it passes through the ramjet engine. The compression process takes the air from its condition at station **a** isentropically to its stagnation state **02** at station **2**. The combustion process is represented by a constant-pressure heat and mass addition process **02** to **04** up to the maximum temperature T_{04}. This maximum temperature is the limiting Mach number due to material temperature limits. Figure 19 shows the temperature of the air as it passes through the ramjet. Finally, the exit nozzle expands the combustion products isentropically to the ambient pressure [Hill, Peterson pg. 151-152]. The ideal engine thrust may be obtained from the following equation:

$$T = ma[(1+f)ue-u]$$

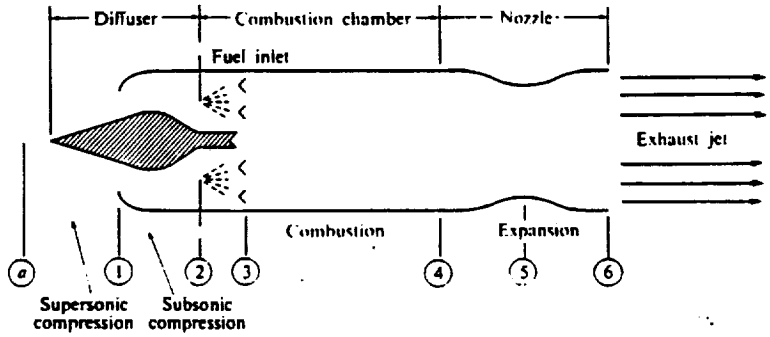

Figure 17: Schematic Diagram of a Ramjet Engine

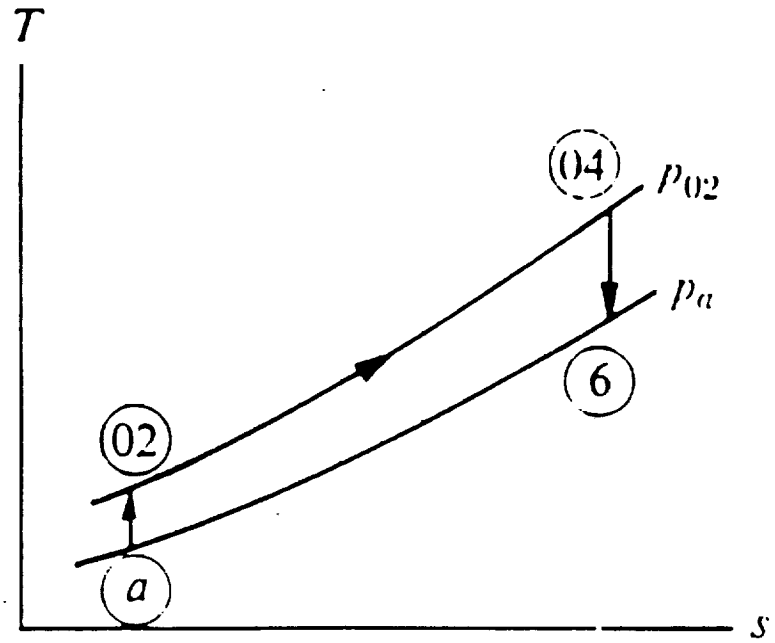

Figure 18: Ramjet T-S Diagram

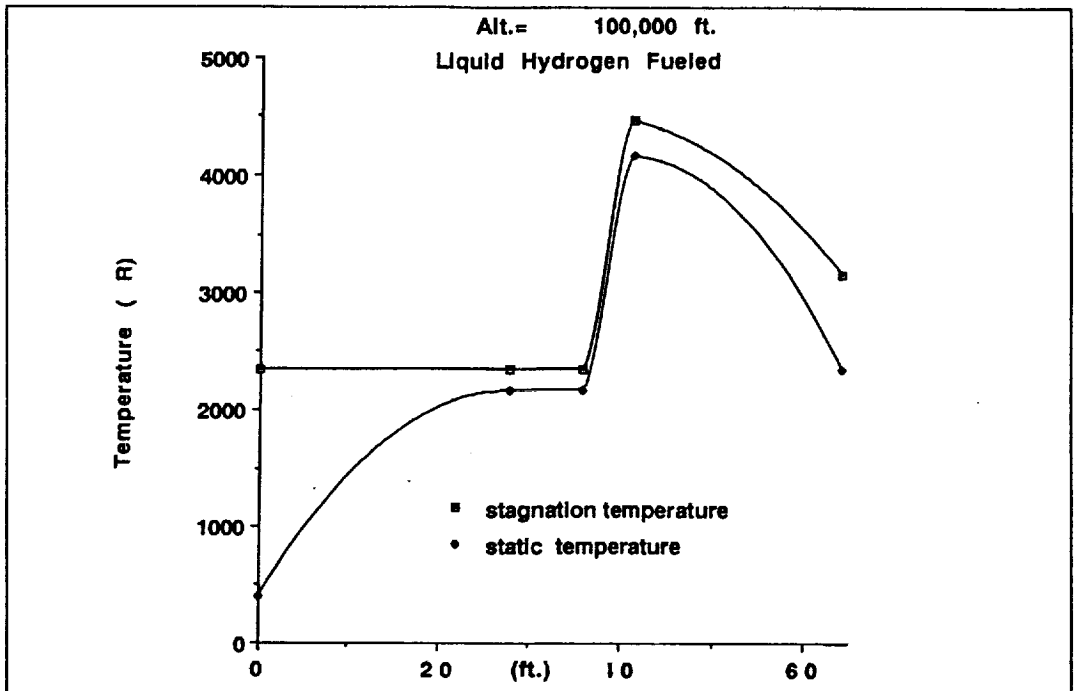

Figure 19: Temperature vs Length of the Ramjet

A program was written to calculate the performance of an ideal ramjet. The performance data was plotted in Figures 20 and 21 which indicate the thrust specific fuel consumption and the required fuel-air ratio of an ideal ramjet as a function of flight Mach number and peak temperature. It can be seen that for any given temperature there is a maximum flight Mach number at which no fuel may be burned in the air. Conversely, it would appear from the Figure 20 that operation at low temperatures is advantageous, since it results in lower TSFC. [Hill, Peterson pg 153]. Figure 22 is a plot of T/ma vs. Mach Number for an ideal ramjet. This plot shows that it is more advantageous to operate at higher temperatures. Obviously, a trade-off must be made as to determine the highest possible operating temperature, but still have low enough fuel consumption.

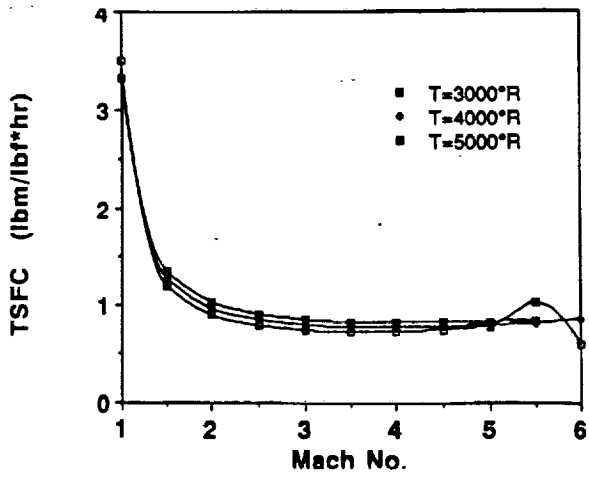

Figure 20: TSFC vs Mach Number

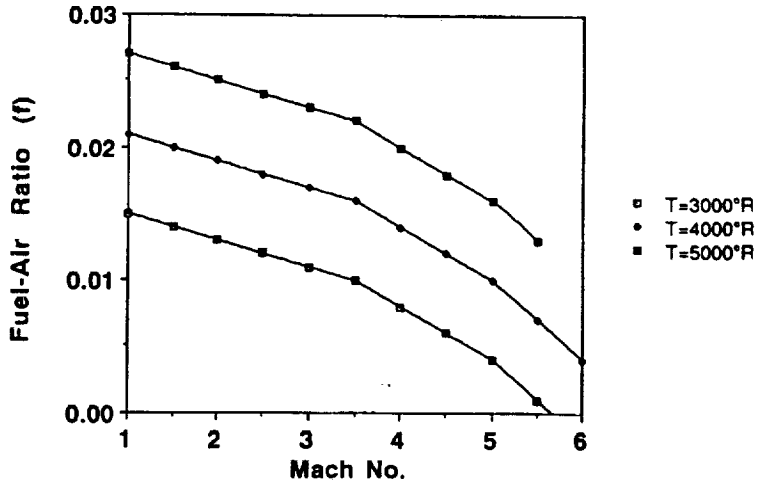

Figure 21: Fuel-air Ratio vs Mach Number

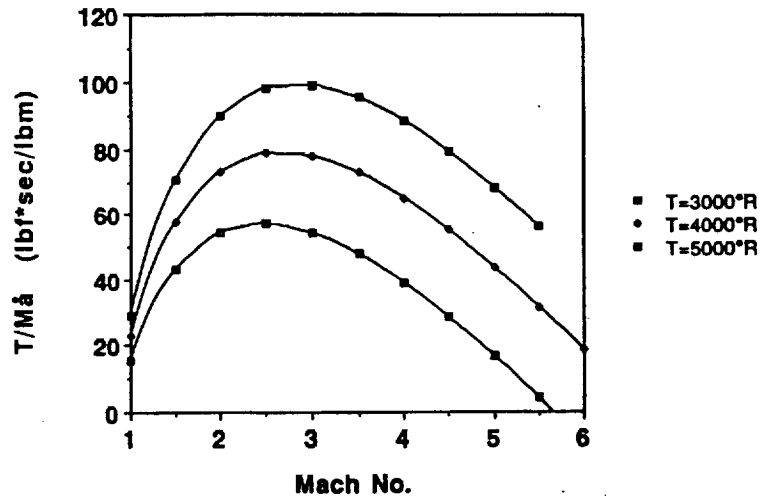

Figure 22: T/ma vs Mach Number

Even though an ideal ramjet is most desirable, an accurate representation of the thermodynamics of the gasses inside the ramjet needed to be investigated. A ramjet program was obtained for Dr. Rudolph Edse that accurately calculates the performance of a ramjet engine. The program is more accurate because the effects of dissociation(changing molecular mass), varying specific heats, and inefficiencies of the thermodynamic processes are taken into consideration. As a result of adding more accuracy, the performance characteristics are diminished due to inefficiencies.

The analysis of the hydrogen powered turbojet was made increasingly difficult due to the fact that no accurate performance program was generated to obtain data. A schematic diagram of a turbojet engine is shown in Figure 23. The thermodynamic process is represented in Figure 24 by a temperature-entropy diagram. As in the

case with the ramjet, the thrust output of the engine is dictated by the maximum allowable temperature of the engine components, specifically the turbine blades.

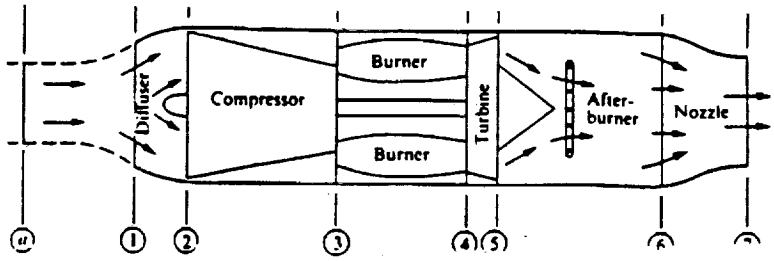

Figure 23: Turbojet Schematic

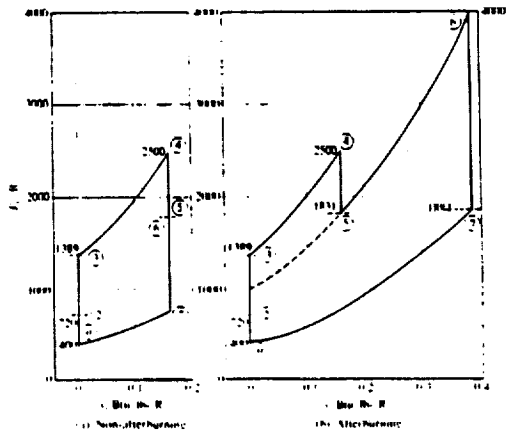

Figure 24: Fluid Processes in the Ideal Turbojet Engine

Since a turbojet program of out own was not generated, the performance data for the turbojet was obtained from the GE engine data. The Mach 6 hydrogen powered wrap around turbojet-ramjet was chosen as the model to be used, with only the turbojet data needed. Figures 25 and 26 show the thrust/air flow rate vs. Mach number and TSFC vs Mach number for the turbojet.

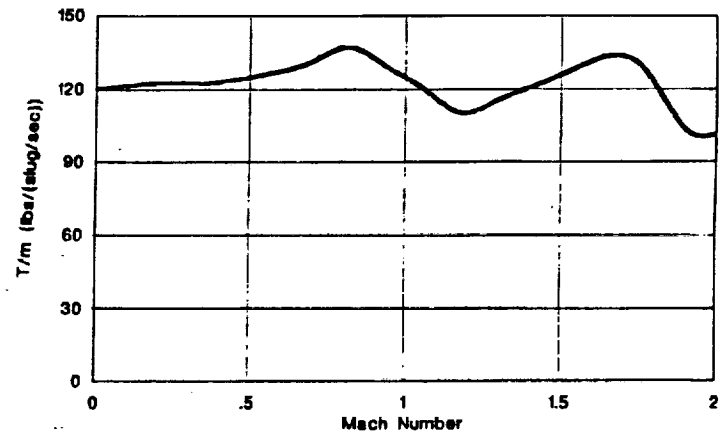

Figure 25: T/ma vs Mach Number - Turbojet

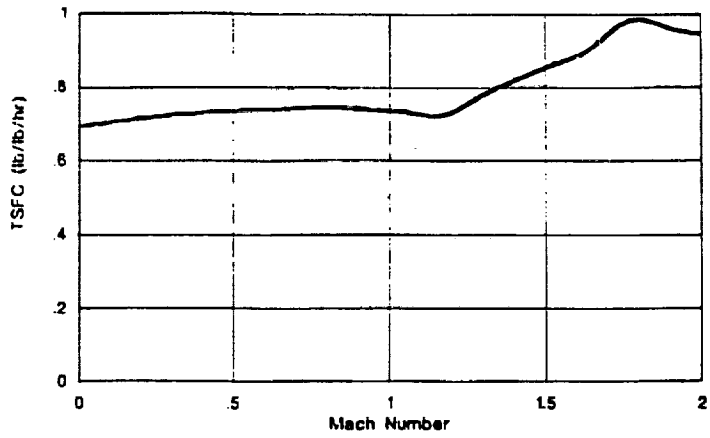

Figure 26: TSFC vs Mach Number - Turbojet

Once the data was obtained for the turbojet and ramjet, the two engines were integrated into a single unit to determine the best range of velocity to convert from the turbojet to the ramjet. By carefully analyzing the specific fuel consumption and the thrust output, Mach 2.5 at approximately 60,000 ft. was selected as the optimum speed and altitude to convert from the turbojet to the ramjet, as seen from Figure 27. Even though the ramjet will be less efficient at this Mach number, the disuse of the turbojet will ultimately save more fuel because of the minimization of afterburning thrust. A cruise Mach number of 5 was selected to try to reduce the amount of active cooling needed between the two engines. Also, since our mission requires changes in altitude a lower cruise velocity minimizes the amount of fuel burned to accelerate to cruise speed.

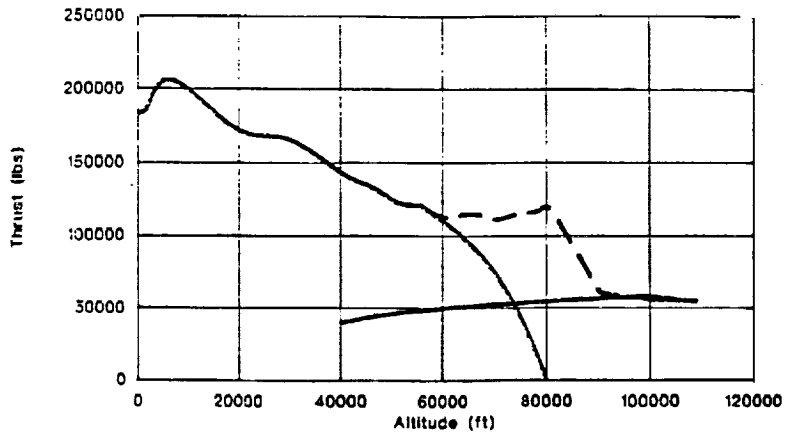

Figure 27: Combined Thrust Available

Figure 28 is a schematic of the integrated turbojet-ramjet configuration selected to propel the aircraft. Notice the turbo engine closure at the forward portion of the compressor stages. This mechanism retracts outward and deflects the airflow through the ram duct and into the ram burner. Since the ram burner is attached behind the turbine section, the extreme temperatures associated with high speed flight not experienced by the turbine blades. In combined operation, the ram burner can also be used as an afterburner. Three engines will be needed to provide enough thrust to overcome the aerodynamic drag and weight of the aircraft. Table 3 shows some of the relative dimensions of the engine configuration and the relative performance data of the turbojet and ramjet. The expansion nozzle uses the entire real portion of the aircraft to expand the gases to as near the ambient conditions as possible. By integrating the performance data between the turbojet and ramjet, the plots of TSFC, thrust available, and power available were plotted versus Mach

number. These plots are presented in Figures 29, 30, and 31. By examining the thrust and power curves, the oversizing of the turbojet is readily apparent. The turbojets were oversized to ensure the takeoff capability of a fully fueled vehicle or to accommodate larger accelerations.

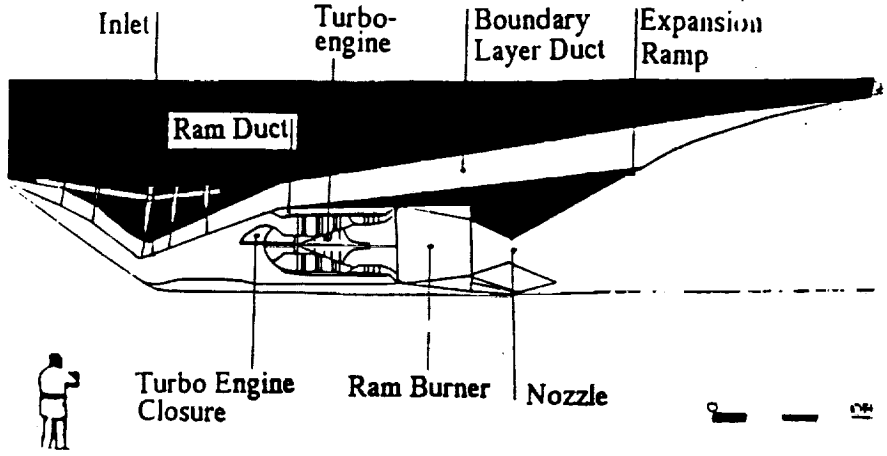

Figure 28: Integrated Turbo/Ramjet Configuration

Table 3: Engine Configuration Data

	Turbojet(S/L T-O)	Ramjet(Cruise)
	Core	Ram burner
Length	7.7 ft.	5.6 ft.
Inlet Diameter.	3.75 ft.	5.67 ft.
Max. Height	4.33 ft.	6.10 ft.
Dry Weight	4000 lb.	1500 lb.
Performance	60,000 lb st.	18,000 lb
Rating		
Specific Fuel Cons.	0.72 lb/hr/lb	0.90 lb/hr/lb

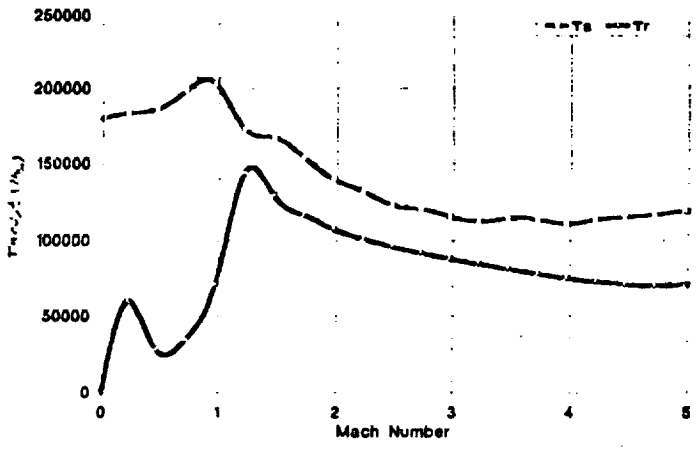

Figure 30: Combined Thrust Available vs Mach Number

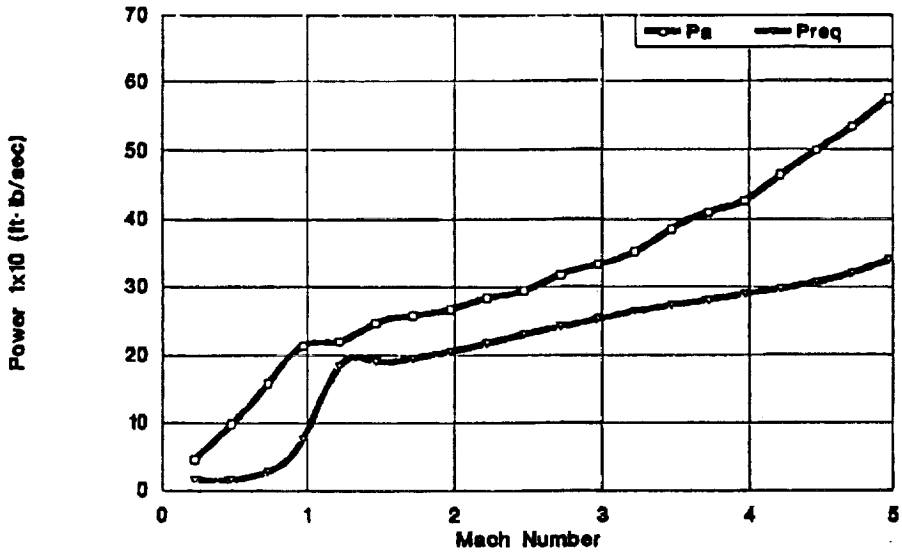

Figure 31: Combined Power Available vs Mach Number

Inlets

The primary purpose of an inlet is to supply the correct quantity and quality of air to the compressor of the engine. The correct mass flow of air must be delivered to the compressor face at a Mach number of about 0.7. The mass flow must also be delivered with an acceptable velocity distribution across the engine face and with minimum loss in the total energy content of air. The inlet should do this at all flight conditions with least weight, cost, and drag. The performance of the inlet is related to the following four characteristics:

1. Total pressure recovery
2. Quality of airflow-distortion and turbulence
3. Drag
4. Weight

The overall value of the inlet is determined by evaluating all of these characteristics because one may be better at the cost of another. Although the inlet analysis codes have not been modified, due to time constraints, the initial characteristics of the inlet can be specified. First, the inlet will be a mixed compression inlet(meaning compression occurs internally and externally to the inlet). This is shown in Figure 32. The compression ramps were found from the FORTRAN code Ramps. The angles correspond to a shock-on-cowl lip criteria so that losses are minimized. Three ramps were chosen for weight savings and simplicity. The lengths of the three ramps are shown in Table 4.

Ramp #	Xloc(ft.)	Yloc(ft.)
1	0.00	0.00
2	9.7	1.7
3	13.0	2.8

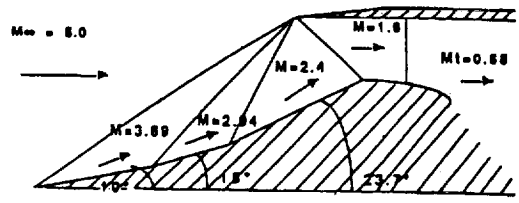

Figure 32: External Compression Ramps

Table 4: Inlet Ramps for the Engine

Ramp #	Xloc(ft.)	Yloc(ft.)
1	0.0	0.0
2	9.7	1.7
3	13.0	2.8

To reduce viscous losses, a boundary layer duct was incorporated into the structure. The required area of the duct is represented in Figure 33. Our engine does not necessarily meet this requirement, but it is a guideline to shoot for.

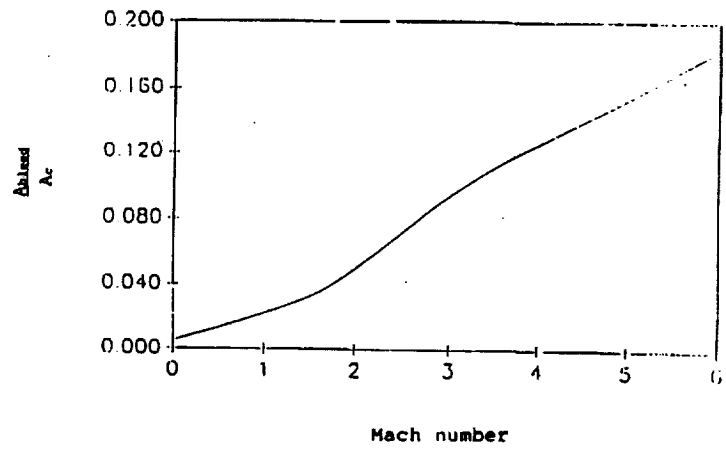

Figure 33: Required Bypass Ratio

Fuel Selection and Management

In selecting the fuel to power the aircraft, the ease of refueling became the driving factor in deciding the fuel. Refueling two types of fuel was inconvenient for

the tanker and too time-consuming for our mission. Liquid hydrogen was selected because it gives more punch for its weight. Also, JP cannot handle the temperature extremes of high speed flight. Methane was considered as an alternate fuel, but it increased the take-off weight as compared to the hydrogen fuel.

The weight distribution over time can be seen in Figure 34. The chart shows that the aircraft begins take-off at a weight of 245,000 pounds. After about a one hour cruise, the aircraft performs an idle power on descent to 40,000 feet from Mach 5 to Mach 2. At 40,000 feet, the aircraft decelerates at a constant altitude to Mach 0.8. At Mach 0.8, the aircraft throttles up the engines for a 5 minute hook-up time with the tanker. The aircraft then refuels approximately 9,500 lbs/min of liquid hydrogen for about 20 minutes before beginning the process again for the 5,000 nautical mile cruise and the final 3,500 nautical mile cruise. The dashed line on the chart represents the empty weight of the aircraft, 136,000 pounds. It can be seen that at each point in the trajectory the aircraft has reserve fuel for a missed approach on landing or missed hook-up with the tanker. As a summary, Figure 35 displays the fuel management for our aircraft.

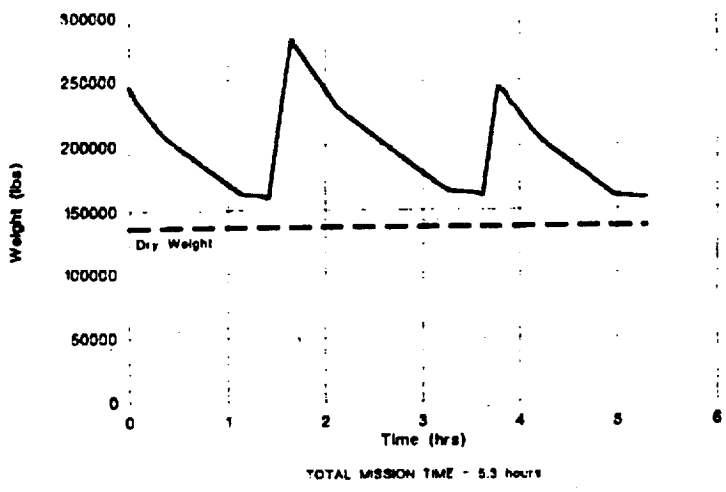

Figure 34: Weight Distribution Over Time

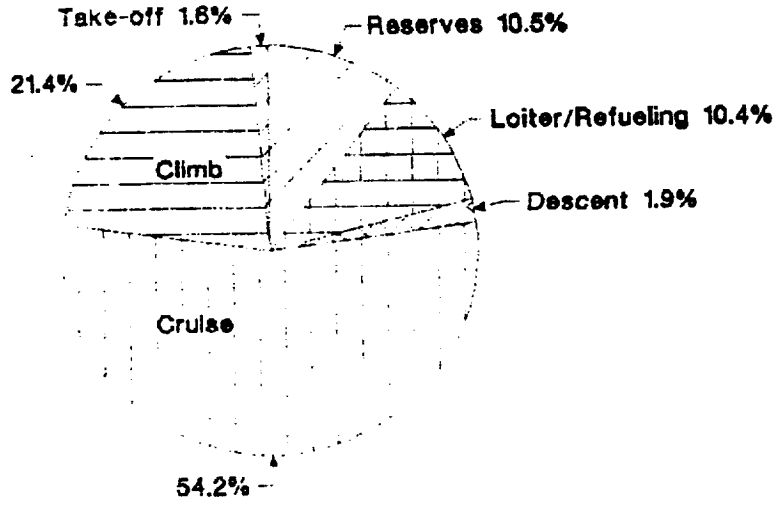

Figure 35: Fuel Management Chart

Engine Materials

The maximum velocity that the aircraft can obtain is Mach 5.6 at 100,000 feet. The propulsion system can propel the aircraft to a much higher velocity, but the internal and external material temperature limitations dictate the maximum Mach number. Our engines contain the latest in material technology. Ceramic and carbon composites lead the way to pushing the material temperature limits to higher extremes.

The turbojet in our propulsion system contains materials that will be used in an advanced military engine. The schematic is found in Figure 36. Notice the use of carbon/carbon composites in the afterburning section. This is the same type of material that is used on the Space Shuttle to resist Earth's atmosphere. Since the ramjet operates at higher velocities, it naturally experiences higher static temperatures. Figure 19 shows the temperature plot along the length of the ramjet. Inside the combustion chamber, the static temperature can be as hot as 4000 °F. To get an idea of how hot that really is, Figure 37 shows the melting point of nickel and aluminum alloys along with the spontaneous combustion of JP fuel. To combat the internal and external temperatures experienced by the propulsion system, the schematic in Figure 38 was created. The candidates of choice were silicon and carbon composites. These materials offered the best life expectancy and machineability while still being able to withstand the temperature extremes. Off course, the hot strut shell, ram duct, and expansion ramp will be coated with oxidation resistant coating.

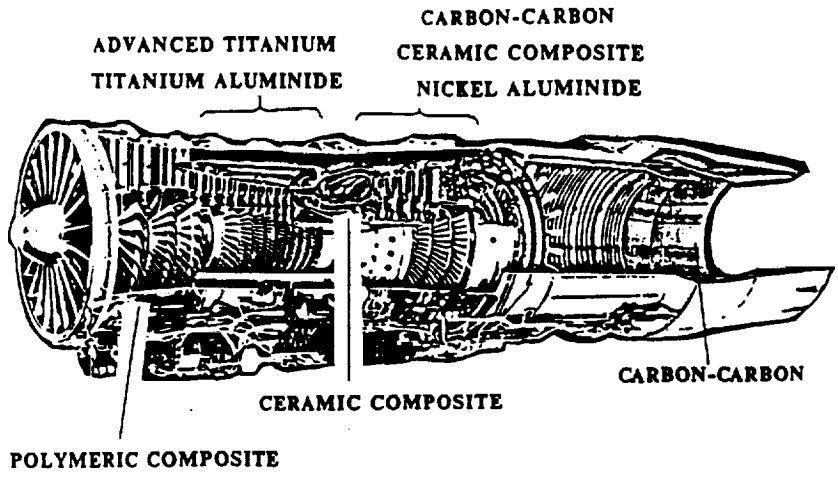

Figure 36: Advanced Turbojet Materials

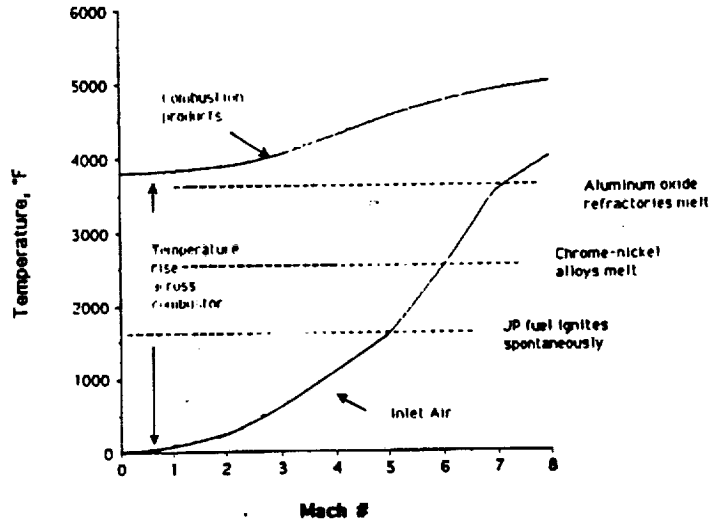

Figure 37: Effect of Dissociation on Ramjet Performance

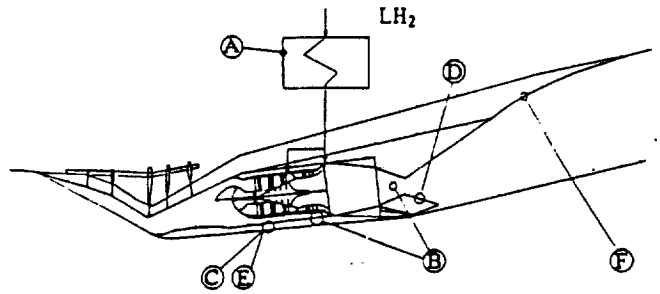

Structures	Material Candidates	Material Surface Temperatures
Ⓐ H_2-Heat Exchanger	C/Cu - alloy	1100°F
Ⓑ Nozzle Casing	SiC/Ti-alloy	1300°F
Ⓑ Ram Duct Casing	SiC/Ti_3Al	1500°F
Ⓒ Hot Strut Shell	TiAl*	1650°F
Ⓓ Nozzle Flaps, Nozzle Cooling Structure	Superalloy	1300* - 2200°F
Ⓔ Hot Strut Shell	SiC/SiC, SSiC	2300°F
Ⓔ Ram Duct Hot Structure	C/SiC*	3100°F
Ⓕ Expansion Ramp	C/C*	3700°F

Figure 38: Ramjet Material Schematic

To help cool the turbojet and ramjet duct while in high speed flight, a fuel heat exchanger will be used. The tubing to carry the fuel will be a carbon/copper alloy that is able to withstand a surface temperature of 1100 °F. The heat exchanger can also be used to cool the inlet structure if needed.

The material temperature limitations are the greatest drawback to achieving extended periods of high speed flight. Hopefully, technological breakthroughs in high temperature, machineable materials will allow projects like NASP to be realized.

AERODYNAMICS

The aerodynamics developed our aircraft were mainly concerned with the trajectory. In order to begin the initial weight and trajectory analysis, a flat plate delta wing configuration was used to calculate lift and drag for the entire flight envelope.This approximation, along with the basic geometry of theaircraft, allowed calculation of values of CDo and the lift curve slope for a given Mach number. In the subsonic and supersonic regions, thin wing theory was used, and these data were curve-fitted to obtain approximations for the transonic region. In order to further simplify analysis, a load factor of 1 was assumed during the climb and descent phases of the trajectory, so the values of CL could be calculated directly from the weight of theaircraft.

During the cruise phase, the aircraft is flown at the optimum L/D. By flying at the optimum L/D, a cruise climb results along with significant fuel savings. The values of CDo and CL obtained from the trajectory were then used to compute CD and L/D, as well as the angle ofattack. These five values were calculated in a subroutine of the main trajectory program, which uses weight, Mach number, and atmospheric conditions as input variables.

From the trajectory, plots of CL, CDo, L/D, and angle ofattack versus Mach number, as well as drag polars, (Figures 39 through 43) were obtained for the first climb to our cruise speed and altitude.

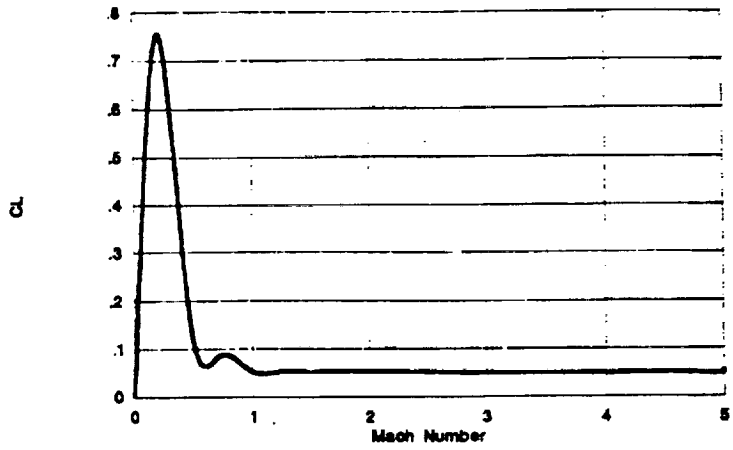

Figure 39: Mission CL vs Mach Number

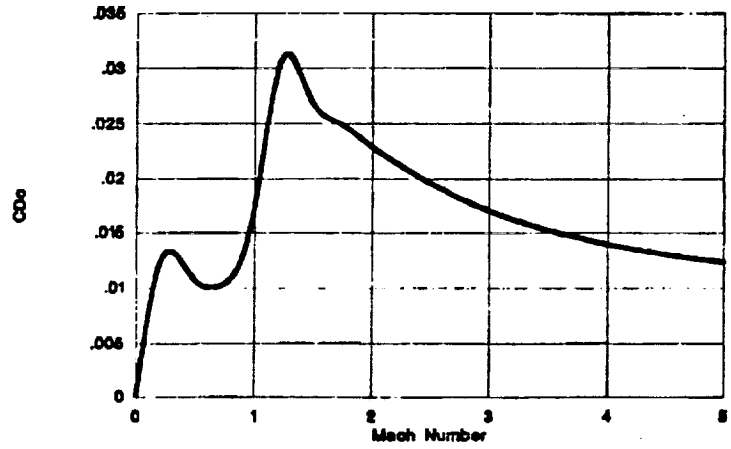

Figure 40: Mission CDo vs Mach Number

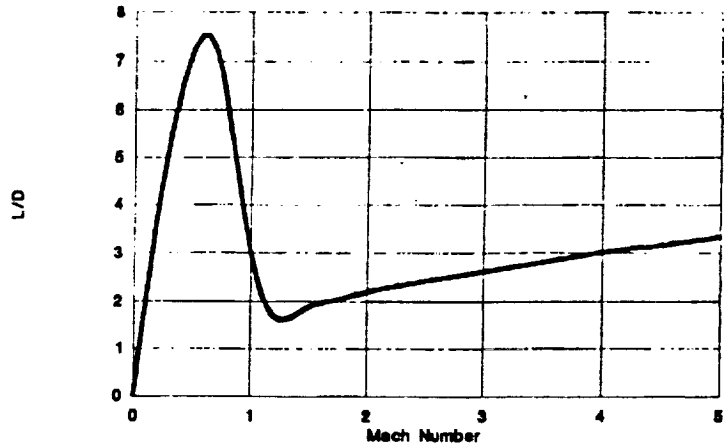

Figure 41: Mission L/D vs Mach Number

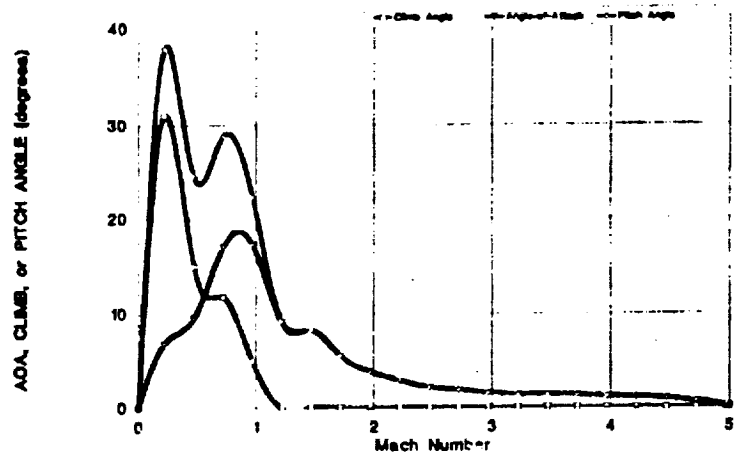

Figure 42: Mission Angle of Attack and Climb Angle vs Mach Number

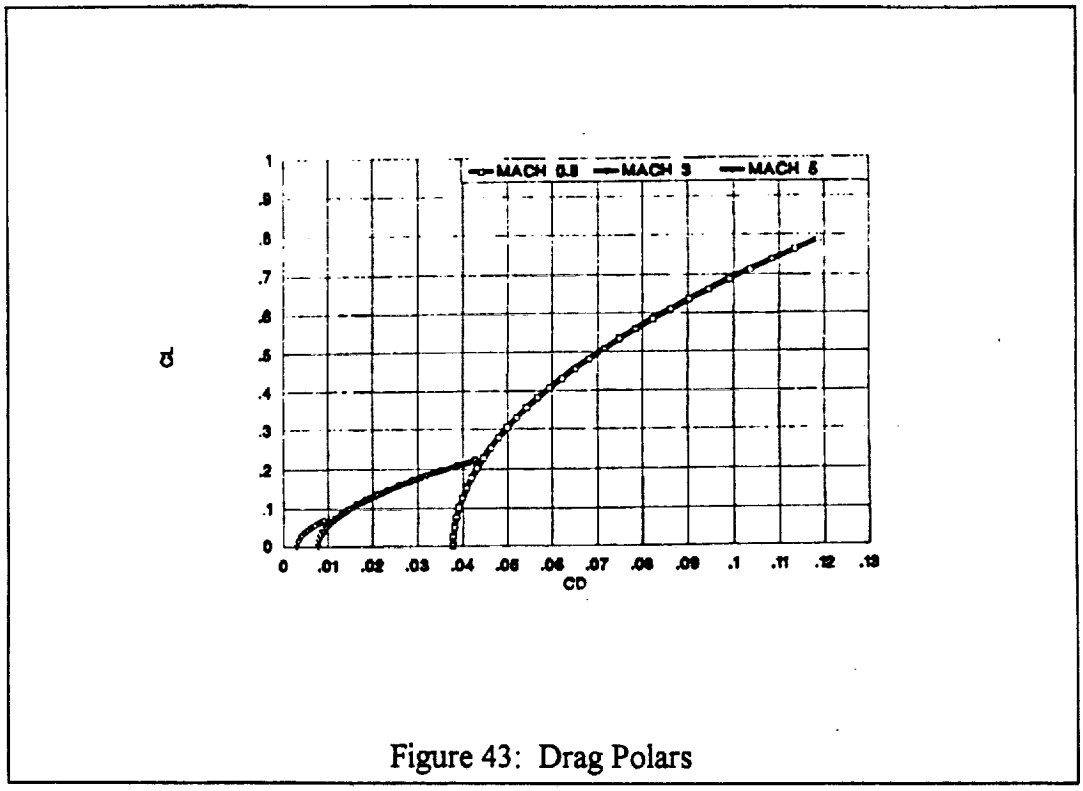

Figure 43: Drag Polars

From these plots, several problem areas may be observed. First, at takeoff, large CLs are required and therefore large angles of attack because of low values of lift curve slope(Figs. 39 and 44). In order to alleviate this problem, a 20% plain flap was considered. As a result the CLmax was increased by 40% and the necessary angle of attack decreased 20 degrees for a 20degree flap deflection (Fig. 45). The addition of flaps also greatly improved our landing performance; stall speed wasreduced 50 knots (Fig. 46) and CLmax increased by 0.8 with a 40degree flap deflection. However, the flaps will not be effective at the refueling speed and altitude of Mach 0.8 and 40,000 feet. As seen in Figure 47, there will be a large change in the angleof attack during refueling.

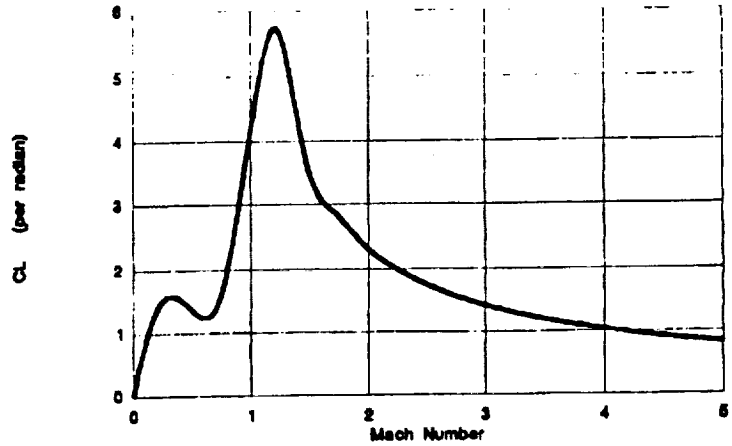

Figure 44: Mission Lift Curve Slope vs Mach Number

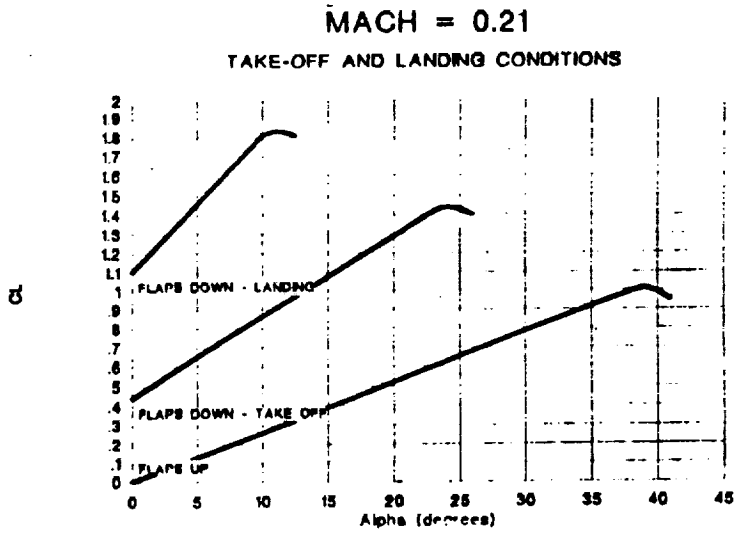

Figure 45: CL vs Angle of Attack

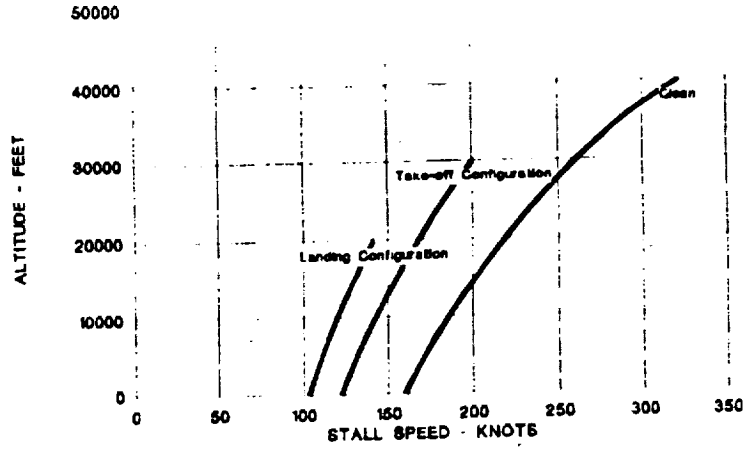

Figure 46: Stall Speed vs Altitude

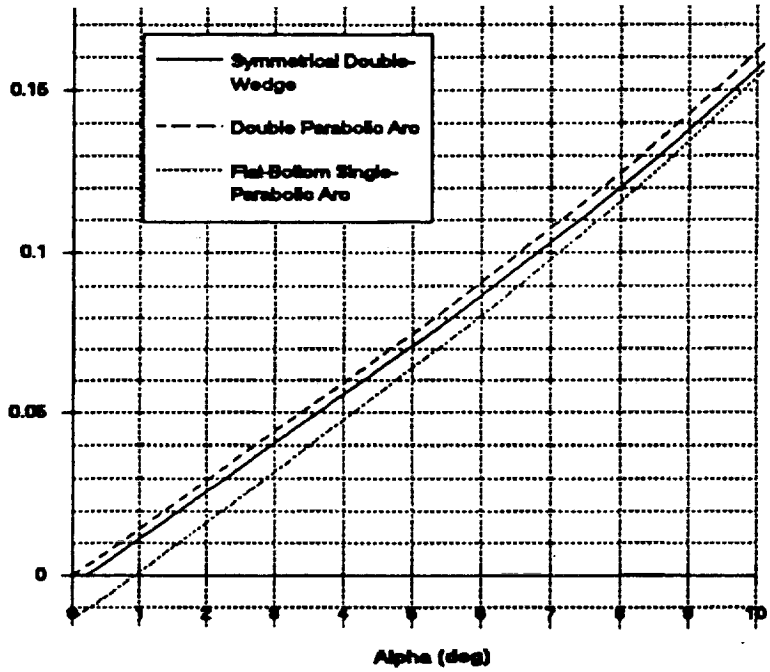

Figure 47: CL vs Angle of Attack at Mach 5

Even though the addition of strakes to the wing will greatly enhance the subsonic lift characteristics (due to vortex lift) and reduce angles ofattack, the problem should be investigated further. The contribution of vortex lift, as well as our selection of an airfoil section, will improve the aerodynamic performance of the aircraft, but were not included in our results due to timeconstraints. The airfoil chosen is a symmetrical double wedge,based on its high L/D at low angles of attack at cruiseconditions and its simplicity in construction. The symmetrical double wedge is compared to other airfoil sections in Figures 48 and 49.

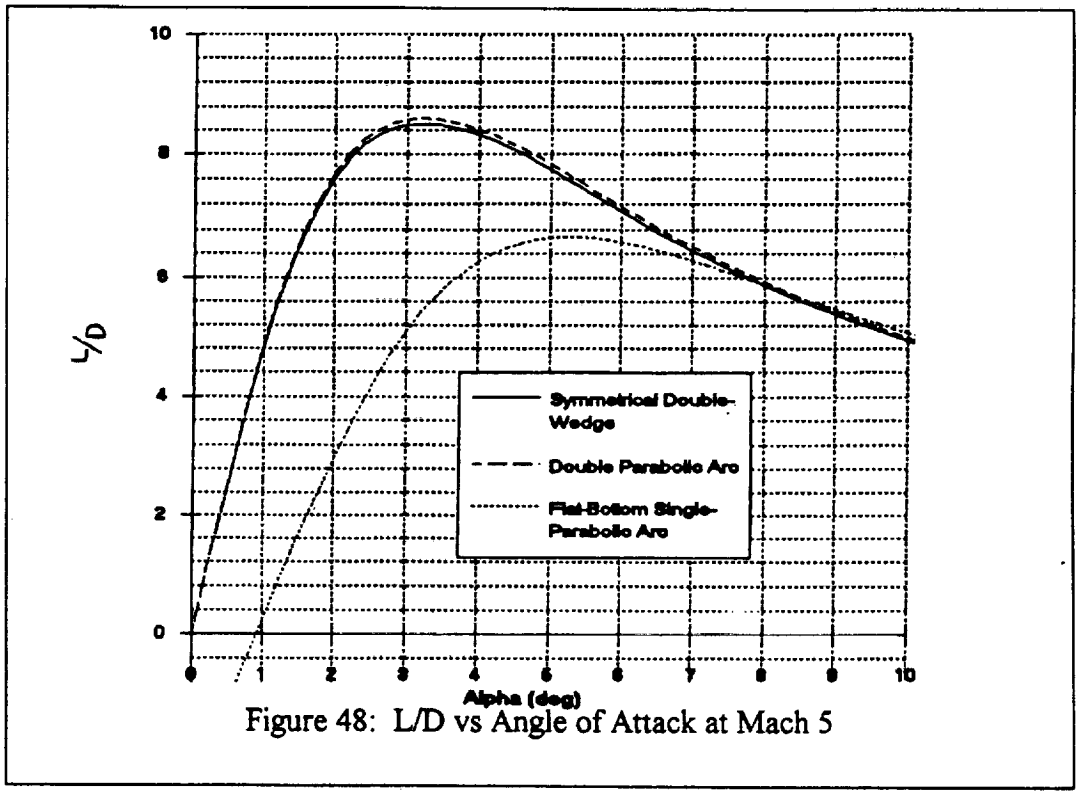

Figure 48: L/D vs Angle of Attack at Mach 5

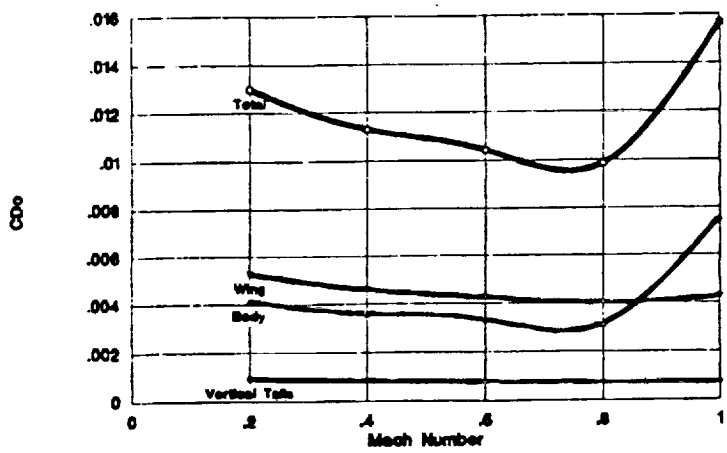

Figure 49: Parasite Drag vs Mach Number (Subsonic)

As the aircraft moves toward the transonic region,a different problem is encountered. At approximately Mach 0.8,the parasite drag increases (and therefore the total drag) dramatically and slowly tapers off in the supersonic region. Inorder to reduce this drag, the strakes which were added are swept such that the leading edges are subsonic in the entire flight regime. As a result, the major contributor to the parasitedrag is the fuselage, as can be seen in Figures 12 through 14. Unfortunately, due to the volume necessary to store fuel, thisdrag cannot be significantly reduced. It should be noted that these calculations were based on fully turbulent flow, but other significant drag sources were ignored, such as the engine box and its integration.

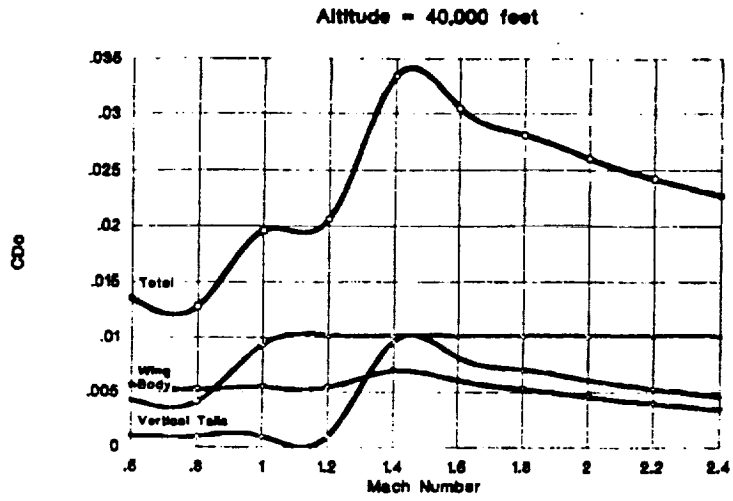

Figure 50: Parasite Drag vs Mach Number (Transonic and Supersonic)

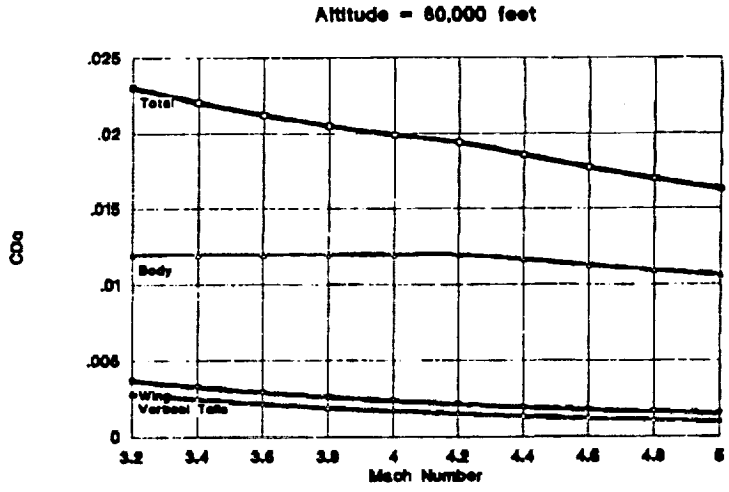

Figure 51: Parasite Drag vs Mach Number (Supersonic and Hypersonic)

STABILITY AND CONTROL

Due to the limited time for this design, the effort in stability and control was concentrated on determining the longitudinal static stability of the aircraft. A statically stable aircraft will tend to return to its undisturbed conditions, thus greatly simplifying the control systems necessary for flight. The analysis was performed only for thesupersonic region of the flight envelope; the high angles of attack in the subsonic region require a more advanced method than the simple linear theory used. For these initial calculations, the contributions of the engines and fuselage to the pitching moment are ignored for simplicity.

The aerodynamic center of the aircraft was found to be 33 feet from the trailing edge of the wing, and the center of gravity to be 120 feet from the nose, and travels less than 4 feet during the entire flight. This results in the center of gravity located approximately 17 feet in front of the aerodynamic center. Without the addition of the strakes, the distance wouldbe almost 30 feet. It is obvious that this distance will cause a large nose-down moment, which must be counteracted by the tail surfaces. The tail surfaces were placed in the V-tail configuration so that both longitudinal and lateral/directional control could be obtained without two sets of control surfaces, thereby reducing the parasite drag. 20 percent elevators were considered for the analysis, and trim deflections were less than 25 degrees. Our initial results indicated that the aircraft is stable (dCm/dangle of attack is negative), but overly so. The static margin was 82% of the chord (approximately 25 feet), well above the desired values of 5 to 15%, so the aircraft would be very difficult to maneuver. This large value could be brought into the desired range by three methods. First, the area of the tailsurfaces could be increased, but this could create unnecessary additional drag if the large area is not necessary for lateral/directional stability. A second method would be the addition of elevons to the main wing. The

most efficient method would be a further attempt to move the aerodynamic center forward, closer to the center of gravity by moving the wing position. This is the most viable option only if the wing is not a major contributor to the total weight of the aircraft; otherwise the center of gravity would move forward along with the aerodynamic center and not improve the static margin.

THERMAL PROTECTION SYSTEMS

One of the major problems which hypersonic vehicles must deal with is the dissipation of heat from the aircraft. In order to avoid structural damage and potential negative effects on vehicle performance, a thermal protection system (which consists of active or passive cooling systems and selected thermal resistant materials) was necessary. Before a trade study on selection of materials and construction for a thermal protection system can be made, a skin temperature contour for the entire aircraft must be found.

First, nose and leading edge temperatures were calculated, and eventually a whole aircraft skin temperature contour was created. The approach used by CDHEAT (a computer program designed to estimate hypersonic aerodynamic heating) was followed to write a FORTRAN program that would calculate temperatures along the entire aircraft. Equations for heat transfer coefficients were used to approximate existing temperature charts for simple aerodynamic shapes in hypersonic flow. The reference heat transfer coefficients were based on a wall temperature near 1600°F (standard day, Mach 5, and 80,000 feet altitude). A low emissivity of 0.7 was used as a safety factor, but the emissivity could be as high as 0.9 for a material such as nickel superalloy. Local Reynold's numbers greater than one-half million were assumed on most of the aircraft in order to model the heat transfer coefficients in turbulent flow. Turbulent flow was assumed along the whole aircraft to simplify calculations and to provide an adequate safety factor over pure laminar flow or mixed laminar and turbulent flow. Wall temperatures were found by an iterative process for convection

$$\text{heat flux} = h_{ref}{}^{*}h/h_{ref}{}^{*}(T_{aw} - T_{w})$$

and radiation

$$\text{heat flux} = \varepsilon * \sigma * T_{w}{}^{4}$$

heat transfer rates in equilibrium for an insulated surface. In order to properly use the above mentioned program, our aircraft was modeled as two delta-wings, a cone, a cylinder, and delta-wings for the tail fins. The program used leading edge analysis to represent the nose, the inlet, the delta-wing leading edges, and the tail fin leading edges. The nose temperature and leading edge temperatures of the main delta-wing (sweep angle 66.5°) and strake (sweep angle 82.5°) were plotted for various Mach numbers at 80,000 feet altitude in Figure 52. The nose cone radius was 3 inches, and the leading edge radius of the delta-wings were 0.25 inches.

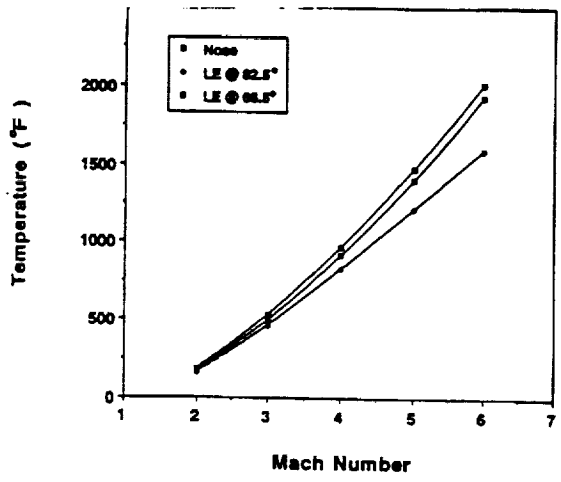

Figure 52: Nose and Leading Edge Temperatures

Since the aircraft was symmetrical about its centerline, the nose cone and airfoil were symmetrical, and the aircraft was subjected to a cruise angle of attack never greater than one degree in hypersonic flight, the top and bottom temperature

contours were basically the same. The skin temperature contour for the aircraft at Mach 5, standard atmosphere, and 80,000 feet altitude is given in Figure 53.

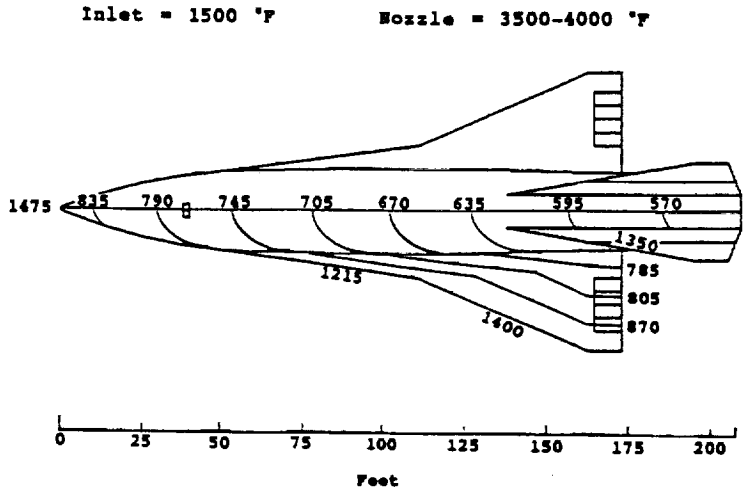

Figure 53: Skin Temperature Contour - Symmetric Top View

Now that temperatures along the entire aircraft were found, an active or passive cooling system must be decided. Under active cooling there are transpiration cooling systems and convection cooling systems.

A transpiration cooling system injects a fluid directly into the boundary layer through the skin. The fluid acts as an insulator which reduces heat flux to the skin. However, the coolant liquid is not recirculated, and that means many thousands of pounds of coolant must be carried. The excess weight and complexities of the coolant distribution system made transpiration cooling an unsatisfactory choice for our particular mission.

A convection cooling system uses the hydrogen fuel or a separate fluid as a coolant which is pumped throughout the skin of the aircraft to serve as a heat sink. A

heat exchanger and complex pumping system must be utilized to allow convective cooling to work effectively. Once again, excess weight and a complex pumping/heat exchanger system with a risk of breakdown made convection cooling an unacceptable choice for our mission.

Passive cooling which involves radiation of heat along an insulated surface was the most attractive choice for a thermal protection system as long as materials can be used to withstand the high temperatures encountered during hypersonic cruise. Looking at the skin temperature contour in Figure 53 once again, the nose, inlet, and all leading edges must withstand temperatures between 1200°F and 1500°F. The exit nozzle must handle temperatures in the range of 3500°F to 4000°F. Finally, the rest of the aircraft must withstand temperatures up to 1000°F. By referring to Figure 54, one can see that alpha titanium alloys possess high specific strengths and creep resistance up to 1000°F. Nickel superalloys possess average specific strengths and a high resistance to oxidation up to 1500°F or even higher when not used as a supporting structure. An oxidation resistant carbon-carbon can also withstand the very high temperatures in the exit nozzle region for a certain number of flights.

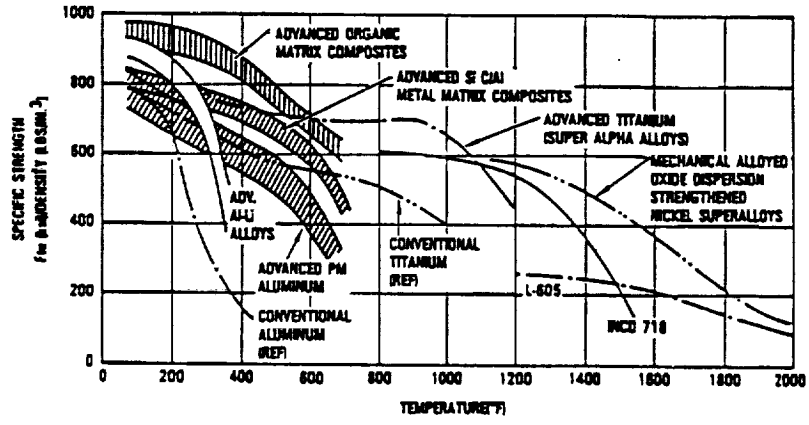

Figure 54: Specific Strength of Materials vs. Temperature

The construction of the heat tolerable skin must take into account the stresses due to temperature effects and to mechanical loads. Wing panels must withstand thermal stresses created by the temperature change through the individual panels, thermal stresses due to temperature gradients through the entire delta-wing, and mechanical stresses from bending, shear, and torsion. For the wing panels and tail fins, a box-stiffened structure as shown in Figure 55 uses titanium webs which were superplastically formed and then diffusion bonded to the Ti-6242Si alpha alloy skin and cap sheets.

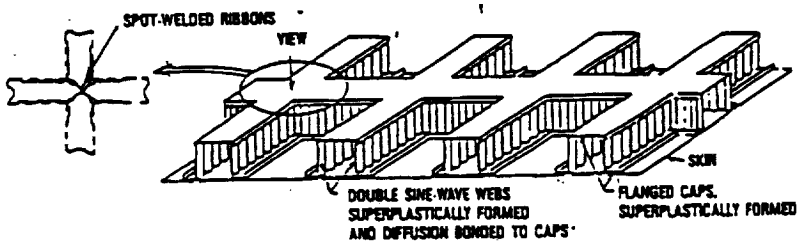

Figure 55: Titanium Wing Panel (Box Stiffened)

For the majority of the fuselage, a radiation-cooled panel made of Ti-6242Si alpha alloy with an insulated substructure was used as in Figure 56. The same

construction was used for the inlets. However, the alpha titanium alloy was replaced by Inconel 617 nickel-based superalloy.

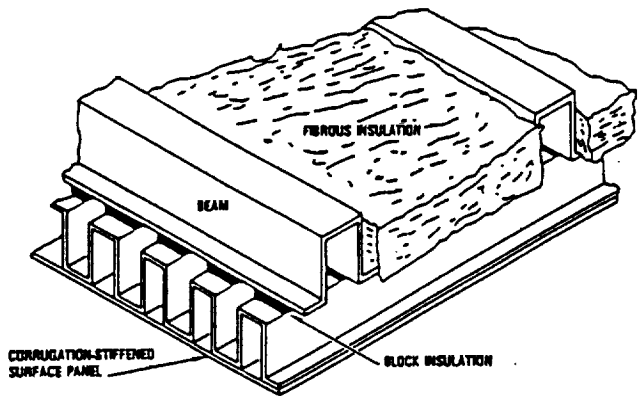

Figure 56: Surface Panel (Radiation Cooled)

For the nose and all leading edges, Inconel 617 nickel-based superalloy was used. A wing leading edge design is presented in Figure 57. The Inconel 617 skin was supported by an Inconel 617 honeycomb structure, and a slip joint was used to allow for thermal expansion relative to the wing panels/box.

Figure 57: Wing Leading Edge Design

Finally for the exit nozzle, an oxidation-resistant carbon-carbon (ORCC) composite was used. This composite has a SiC coating which creates a thin layer of silica glass when exposed to high temperature oxygen and slows the rate of oxidation. This means that the ORCC composite must be replaced around every 20 flights or so, however.

Using these materials as a passive cooling system gave a temperature limit of the aircraft near Mach 5.4 at 80,000 feet altitude.

LANDING GEAR

Tricycle landing gear has been used for this design due to its inherent tip-over stability and proven performance. The two main gear are of the twin tandem type, and the nose gear is of the tandem type. The main gear is positioned so as the forward most contact point lies 30 degrees behind the center-of-gravity at take-off. The tail cone clearance angle is 20 degrees and produces approximately nine feet minimum ground clearance with full deflated gear. This allows 100 feet between the nose gear and the engine intakes to prevent runway debris from entering the intakes. The nose gear retracts forward and the main gear folds back. The main gear boogies swing forward on ramps as the gear enters the housing. The nose gear supports 35.7% of the aircraft weight and the main gear support 64.3%. Figure 58 shows details of the nose and main landing gears.

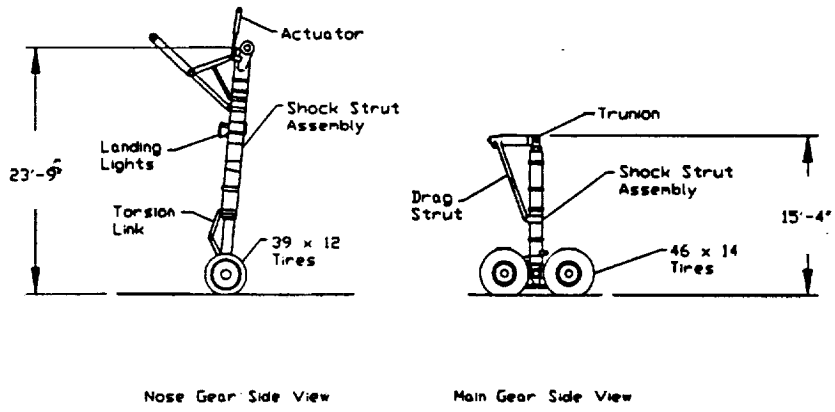

Figure 58: Landing Gear Detail

CRYOGENIC FUEL SYSTEM

Liquid hydrogen tanks are subjected to extreme temperatures during hypersonic flight operations. The flow of air around tanks containing hydrogen at 22 Kelvin creates a problem called cryopumping. At some depth in the insulation surrounding the tanks, the temperature is low enough to condense air. Due to the volume change associated with this phase change, the insulation acts as a vacuum pump and continues to liquefy air (cryopumping). This liquefied air will freeze on the tank wall and increase the heat flux.

Cryopumping creates a number of problems concerning the liquid hydrogen tanks. Cryopumping releases the heat of condensation of air at a high rate inside the insulation. The resulting heat transfer is enough to vaporize fuel at a rate of 18 lbs./hr. per square foot of tank surface area. In addition to the vaporization of fuel, liquefied air causes the accumulation of water and liquid oxygen in the structure, which can have explosive results.

In order to combat the problem of cryopumping, air must be excluded from around the liquid hydrogen tank's walls. Several methods have been suggested for this. Since helium is the only gas that will not freeze at the temperatures encountered by the liquid hydrogen tanks, one solution would be to surround the tanks with a layer of helium gas. However, the diffusion of helium around the tanks would be costly and some systems have been suggested that weigh less and are less costly. Other systems, such as vacuum wall tanks and sealed insulation, have been discussed, but to date the success of these approaches is questionable. An economically feasible solution to the cryopumping problem seems to be a Carbon Dioxide Frost System.

The Carbon Dioxide Frost System (Carbon Dioxide Purge) takes advantage of the fact that carbon dioxide has no liquid phase at the pressures that will be

encountered around the tank. Air is purged from around the tank by carbon dioxide gas during pre-flight preparation. The tank is filled with liquid hydrogen. Then some of the carbon dioxide gas condenses (as frost) within the insulation. After take-off, sublimation of the frost occurs naturally because of the change in pressure with altitude and due to aerodynamic heating. This sublimation of frost provides the purge gas necessary to prevent airflow through the unsealed structure during hypersonic flight (Figure 59). In short, the carbon dioxide gas pushes air away from the tanks, and without air, cryopumping cannot occur.

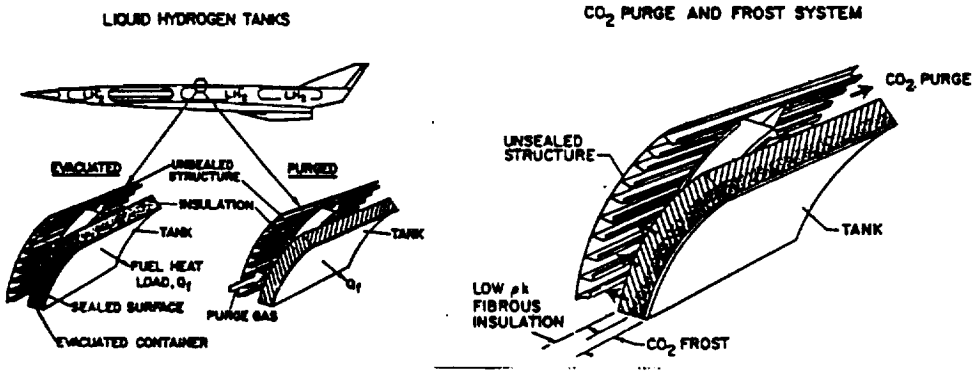

Figure 59: CO2 Purge and Frost System

There are a few problems with the carbon dioxide purge system. First, helium must be used to regulate the thickness of the carbon dioxide frost when it is deposited in pre-flight. As noted earlier, helium is expensive and this adds to the operating cost of the aircraft. Second, studies of similar aircraft show that deposition time of the

carbon dioxide frost requires about one hour. This adds to total mission time. Finally, for subsonic flight, before the carbon dioxide sublimates, a nitrogen gas purge system is necessary to prevent airflow in the insulation. This adds to the weight and complexity of the aircraft. However, these three problems are minor compared to the cryopumping problem that has been eliminated by using the carbon dioxide gas purge system.

AIRCRAFT COSTS

There are three main costs concerning the hypersonic reconnaissance aircraft: 1) Development, Testing, and Evaluation Costs, 2) Production Costs, and 3) Operational Costs. The first category, Development, Testing, and Evaluation Costs, was estimated from a procedure included in Nicolai's *Fundamentals of Aircraft Design*. These costs included airframe engineering, development support, flight test aircraft, and flight test operations. The estimated costs for two development aircraft are as follows:

Table 5: Total DT & E Costs (in millions)

Airframe Engineering	$ 4,150
Development Support	3,100
Flight Test Aircraft	
Engines	40
Manufacturing Labor	540
Material & Equipment	60
Tooling	1,600
Quality Control	70
Flight Test Operations	380
Subtotal	$ 9,940
Profit (10% of Subtotal)	994
Total DT & E Costs	$ 10,930

The second category was Production Costs. This division included engines, labor, material, tooling, and quality control for a total of twelve aircraft. The total production costs for twelve aircraft are as follows:

Table 6: Total Production Costs (in millions):

Engines	$ 180
Manufacturing Labor	850
Material and Equipment	190
Sustaining Engineering	1,610
Tooling	610
Quality Control	110
Subtotal	$ 3,550
Profit (10% of Subtotal)	355
Total Production Costs	$ 3,910

This cost, added with DT & E, represents the total cost of producing twelve hypersonic aircraft. When the total price is divided by twelve, a unit price of 1.2 billion dollars results. This is excessive, but the only design constraint on costs was placed on operational costs. These costs were again approximated from Nicolai. For a fleet of twelve planes making eighty flights yearly, the operational costs were found to be:

Table 7: Operational Costs

Fuel	$ 180.0
Depot and Overhaul	54.0
Spares	45.0
Maintenance	2.4
TPS Replacement	1.0
Crew	0.3
Total Operational Costs	$ 282.7

The operational costs amount to 282 million dollars per year, well under the design criteria of 300 million dollars per year in operational costs.

WIND TUNNEL TESTING

A 1/128th scale model of the aircraft was hand-made using balsa wood and pine plywood. The fuselage was carved to the correct shape from one solid piece of balsa wood, and the wing and V-tail were 1/8th inch thick plywood. The leading and trailing edges were sharpened to simulate the double-wedge shaped airfoil. The engine box was not modeled. The model was suspended in the Ohio State University Low Speed Wind Tunnel. Figure 60 shows how the model was suspended from the test mount.

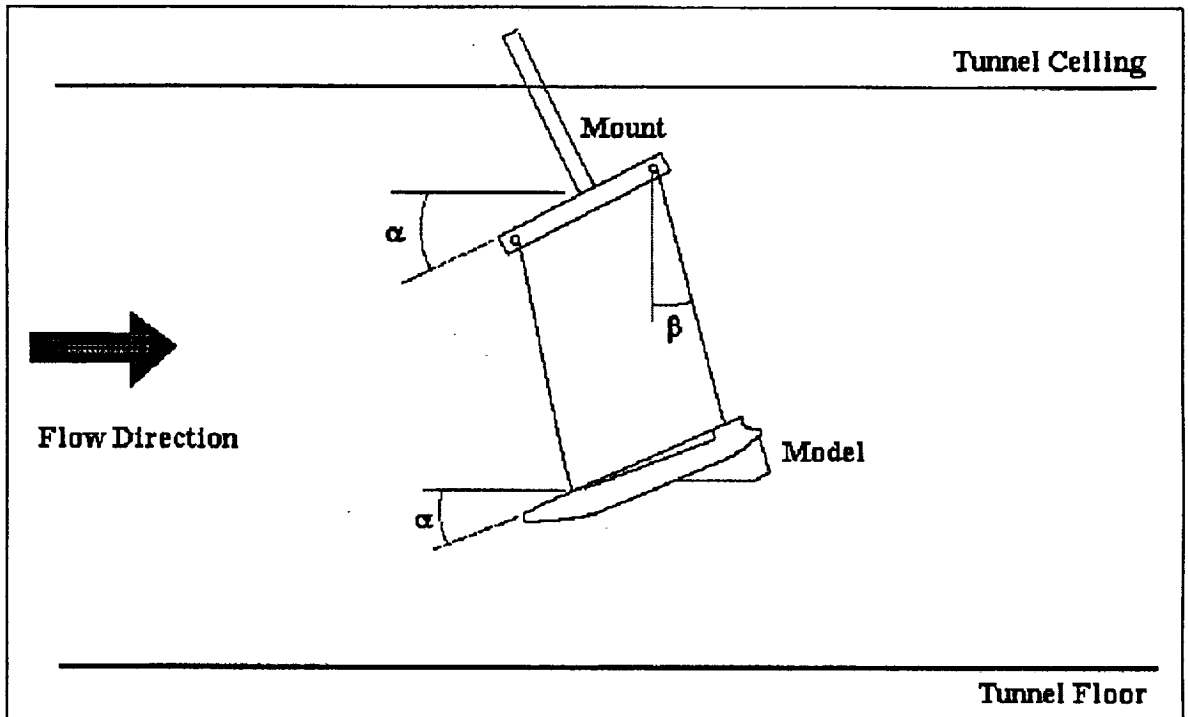

Figure 60: Model Mounting System

As the velocity of the airflow was increased the angle b increased. The change in the angle of the wires was measured for each new velocity. As can be seen from equation 6 in Appendix, the angle b will reached a maximum value as the velocity became large. This maximum value corresponded with L/D_{max}. All raw and

calculated data are included in the Appendix. The results obtained were consistent with calculated values. The following is a plot of L/D_{max} versus AOA:

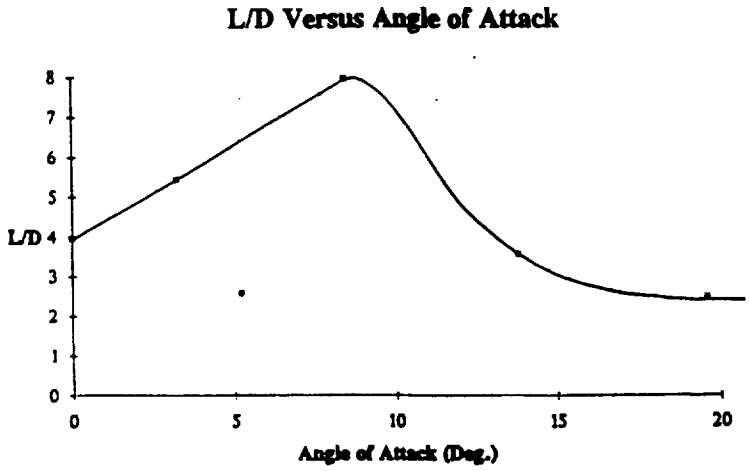

Figure 61: Model L/D vs Angle of Attack

Flow visualization tests were also performed. As was expected, the vortices from the strakes and main wing provided substantial amounts of lift. The nose vortices did not burst before reaching the V-tail. This will help directional control at low speeds.

APPENDIX: WIND TUNNEL DATA

Derivation of force equation:

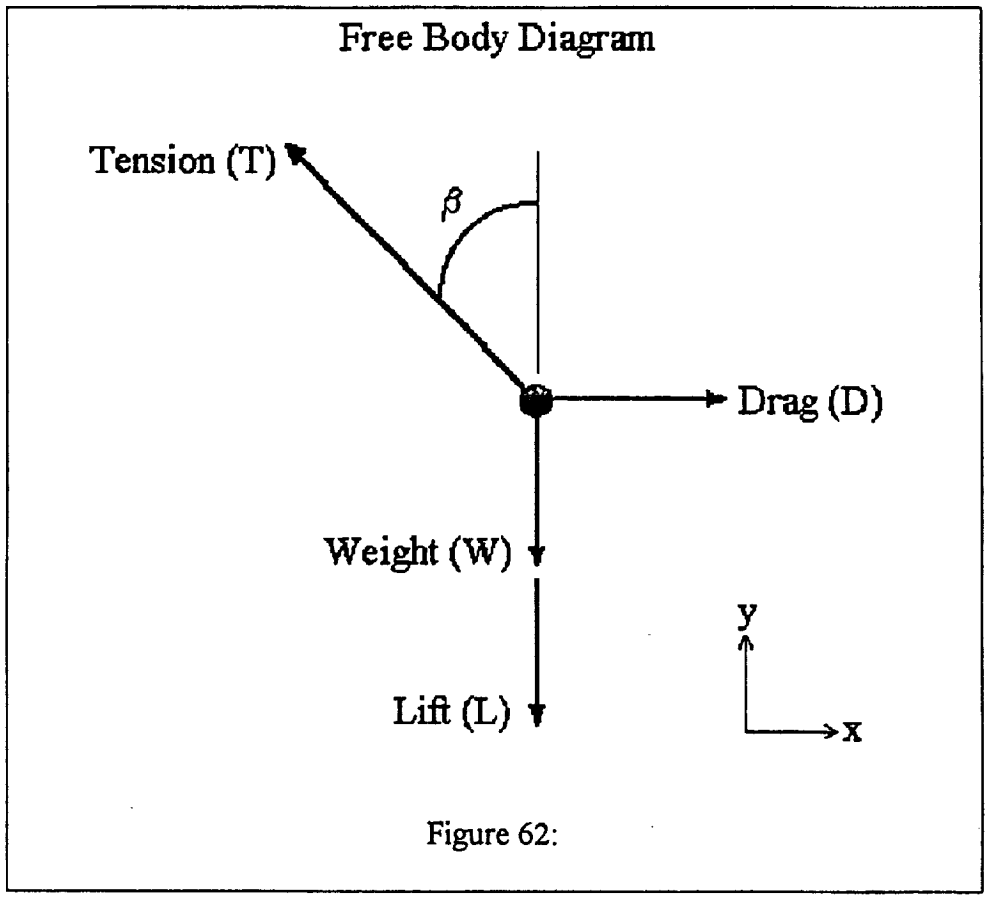

Figure 62:

$$\sum F_x = D - T\sin\beta = 0 \qquad \text{eq. (1)}$$

$$\sum F_y = T\cos\beta - W - L = 0 \qquad \text{eq. (2)}$$

using eq . (1):

$$D = T\sin\beta$$

$$\therefore \; T = \frac{D}{\sin\beta} \qquad \text{eq (3)}$$

substituting eq . (3) into eq . (2):

$$\frac{D}{\sin\beta}\cos\beta - W - L = 0$$

$$D\cot\beta - W - L = 0$$

$$\cot\beta - \frac{W}{D} - \frac{L}{D} = 0$$

$$\frac{L}{D} = \cot\beta - \frac{W}{D} \qquad \text{eq (4)}$$

Results:

Raw Data **Processed Data**

Alpha = 0 deg

x	q
0.75	0.17
1.3	0.311
2.45	0.722
3.35	0.988
4.2	1.292
5.15	1.648

cot B	1/q
64.67	5.88
37.31	3.22
19.80	1.39
14.48	1.01
11.55	0.77
9.42	0.61

Alpha = 3.17 deg

x	q
1.55	0.314
2.325	0.5
2.8	0.725
3.95	1.3
4.8	1.662
5.375	2.058

cot B	1/q
31.29	3.18
20.86	2.00
17.32	1.38
12.28	0.77
10.10	0.60
9.02	0.49

Alpha = 5.2 deg

x	q
1.175	0.313
2.05	0.496
2.775	0.716
3.5	0.985
4.05	1.291
4.65	1.635
5.35	2.03
5.5	2.235

cot B	1/q
41.28	3.19
23.66	2.02
17.48	1.40
13.86	1.02
11.98	0.77
10.43	0.61
9.07	0.49
8.82	0.45

Alpha = 8.397 deg

x	q
1.85	0.0168
3.05	0.309
4.775	0.71
5.625	0.975
6.3	1.275
6.9	1.62
7.45	2
7.85	2.46

	cot B	1/q
bad point	26.22	59.52
	15.90	3.24
	10.16	1.41
	8.62	1.03
	7.70	0.78
	7.03	0.62
	6.51	0.50
	6.18	0.41

Alpha = 13.8 deg

x	q
2.6	0.161

cot B	1/q
18.65	6.21

4.3	0.303
5.85	0.483
6.95	0.707
7.85	0.956
8.85	1.25
9.5	1.598
10	1.995
10.2	2.116

11.28	3.30
8.29	2.07
6.98	1.41
6.18	1.05
5.48	0.80
5.11	0.63
4.85	0.50
4.75	0.47

Alpha = 19.6 deg

x	q
2.15	0.066
4.95	0.161
7.4	0.299
9.25	0.471
11	0.683
12.325	0.945
13.2	1.236
14.15	1.57
14.75	1.94
15.05	2.365
15.35	2.57

cot B	1/q
22.56	15.15
9.80	6.21
6.55	3.34
5.24	2.12
4.41	1.46
3.94	1.06
3.67	0.81
3.43	0.64
3.29	0.52
3.22	0.42
3.16	0.39

L/D vs. Angle of Attack

Alpha	L/D
0	3.94
3.17	5.44
5.2	2.57
8.4	7.95
13.8	3.56
19.6	2.49

Note : All x in inches, q in mm HG, 1/q in $(\text{mm Hg})^{-1}$, Alpha in degrees.

Data Analysis:

Best fit lines were obtained for the processed data points using a linear regression. L/D was obtained using the force equation (eq. 4). The following is a derivation of the L/D equation:

Note: b_{max} is the angle at which the model has traveled its maximum distance backwards. This corresponds with the D >> W, velocity squared approaching infinity.

$$\frac{L}{D} = \cot\beta - \frac{W}{D} \qquad \text{eq. (5)}$$

$$L = c_L S q_\infty$$
$$D = c_D S q_\infty$$

substitute above two equations into eq. (5):

$$\frac{c_L S q_\infty}{c_D S q_\infty} = \cot\beta - \frac{W}{c_D S q_\infty}$$
$$\frac{c_L}{c_D} = \cot\beta - \frac{W}{c_D S q_\infty}$$

taking the limit as q_∞ approaches ∞:

$$\frac{c_L}{c_D} = \cot\beta_{max}$$

$$\therefore \frac{L}{D} = \cot\beta_{max} \qquad \text{eq. (6)}$$

Slope, intercept data, and L/D are given for each AOA in the following table:

Table 8: Wind Tunnel Results

Alpha (deg.)	slope (1/mm Hg)	y-intercept (1/mm Hg)	L/D
0	0.09643	-0.38037	3.94
3.17	0.12340	-0.67116	5.44
5.2	0.85757	-0.22033	2.57
8.397	2.7290	-21.6890	7.95
13.8	0.4155	-1.4777	3.56
19.6	0.76677	-1.9085	2.49

Data Plots (processed data):

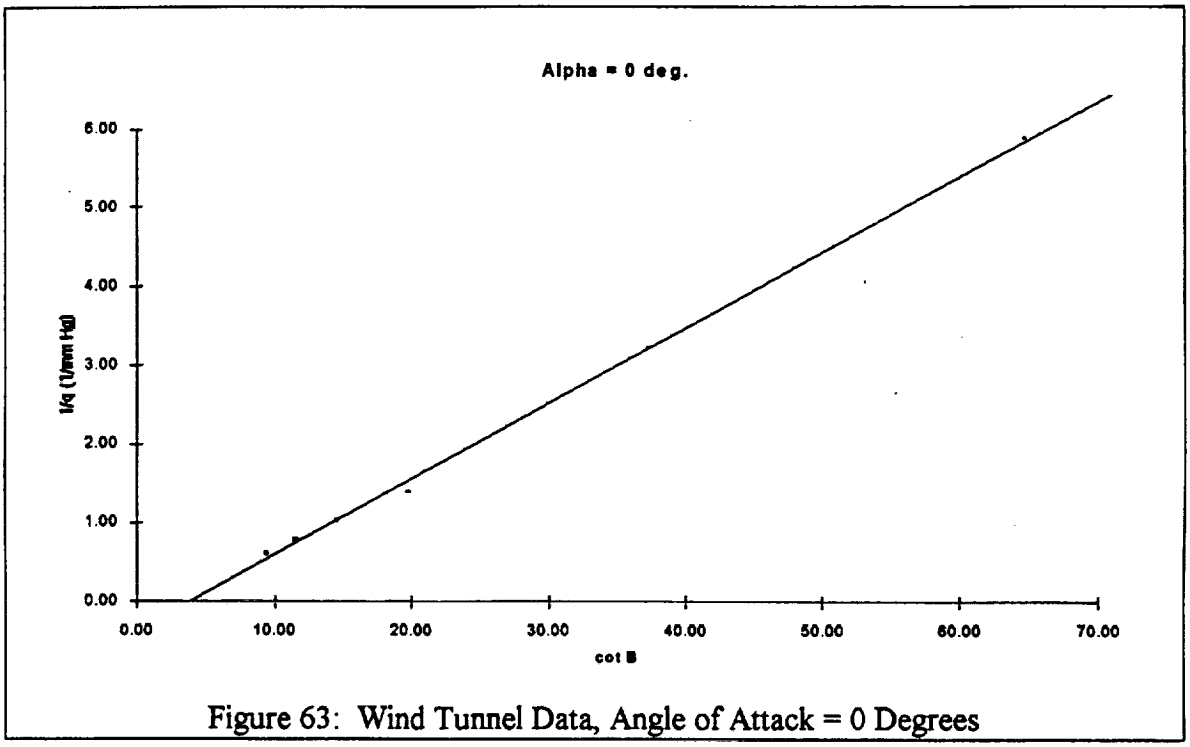

Figure 63: Wind Tunnel Data, Angle of Attack = 0 Degrees

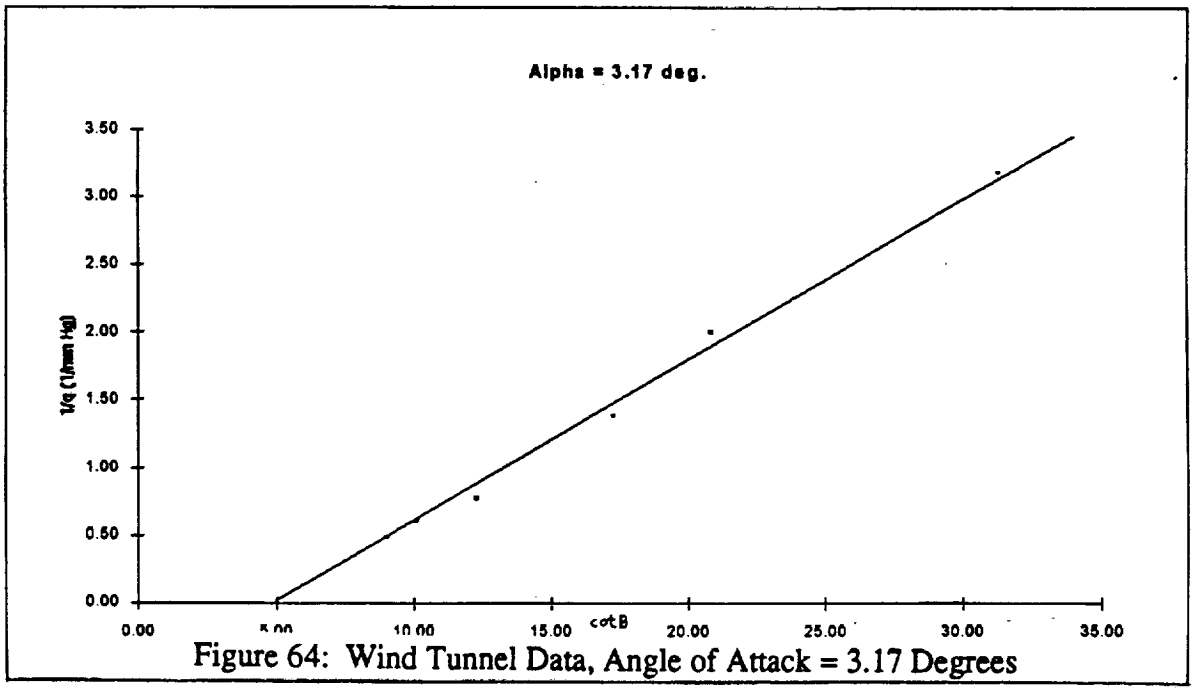

Figure 64: Wind Tunnel Data, Angle of Attack = 3.17 Degrees

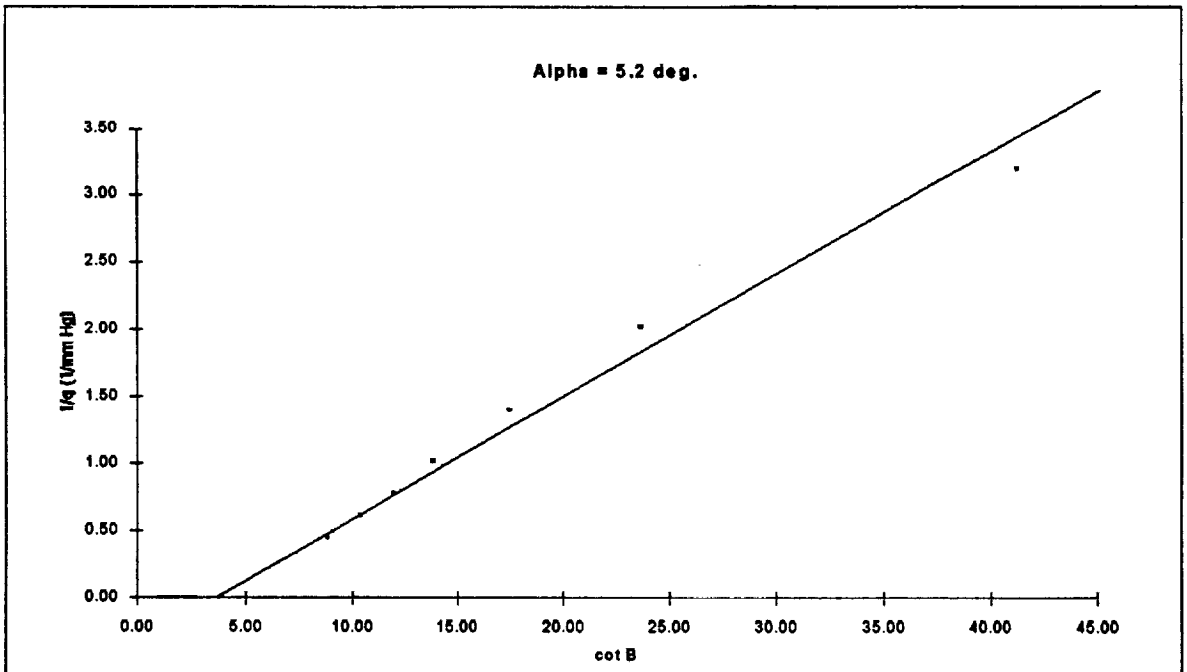

Figure 65: Wind Tunnel Data, Angle of Attack = 5.2 Degrees

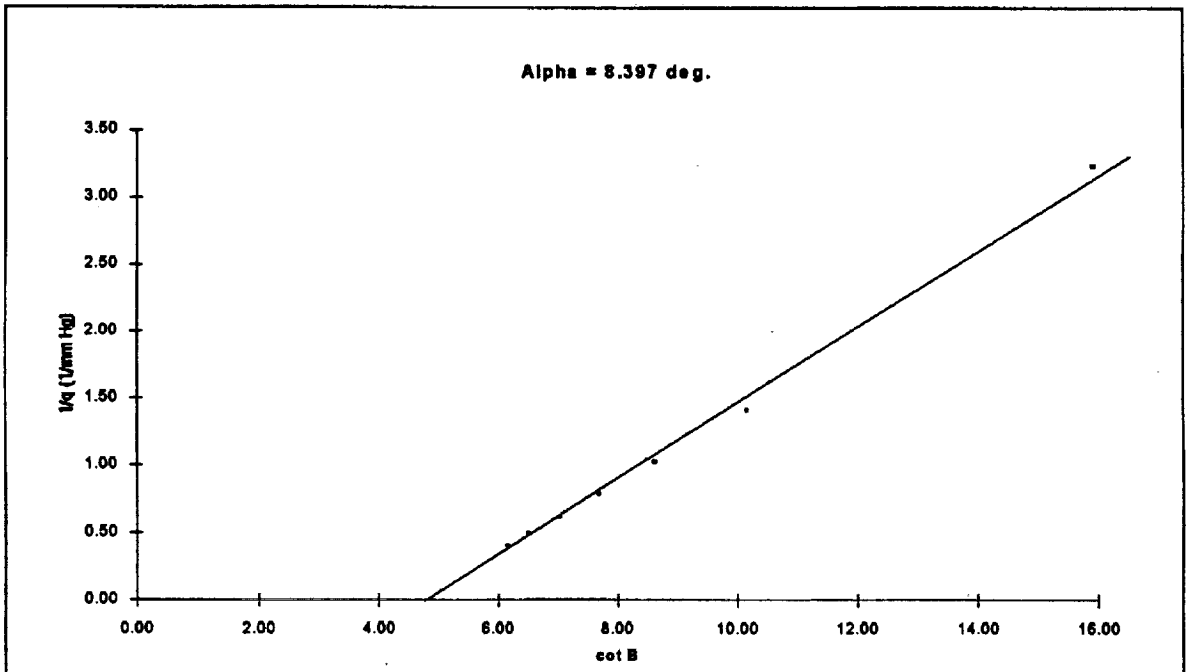

Figure 66: Wind Tunnel Data, Angle of Attack = 8.4 Degrees

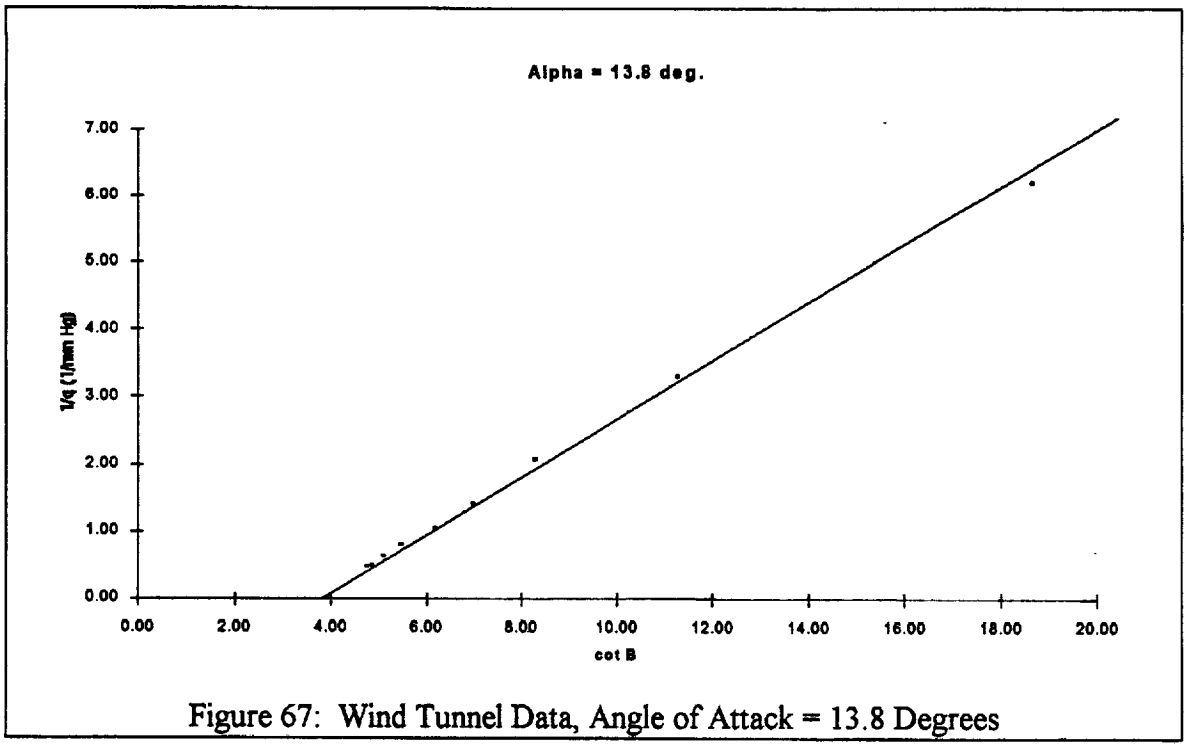

Figure 67: Wind Tunnel Data, Angle of Attack = 13.8 Degrees

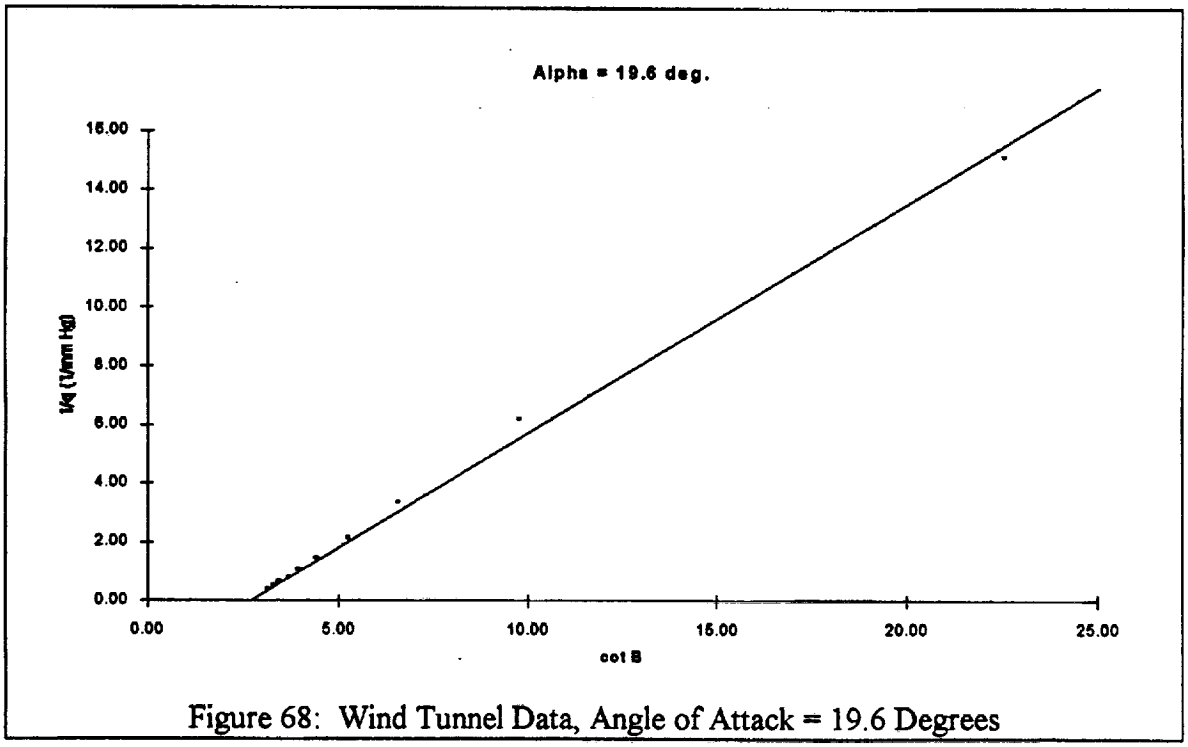

Figure 68: Wind Tunnel Data, Angle of Attack = 19.6 Degrees

REFERENCES

Raymer, Daniel P., *Aircraft Design: A Conceptual Approach*, American Institute of Aeronautics and Astronautics, Washington, DC, 1989.

Hill and Peterson, *Mechanics and Thermodynamics of Propulsion*, Addison-Wesley Publishing Company, Reading, Massachusetts, 1970

Nicolai, *Fundamentals of Aircraft Design*, METS, Inc., San Jose, California, 1984

German Hypersonics Technology Programme, Status 1991, 42nd Congress of the International Astronautical Federation (IAF), Montreal, Canada, October 1991, Paper No. IAF-91-198

Dreshfield, Robert L., "Advanced Materials for Long-Life Applications", Materials Division, NASA Lewis Research Center

Jackson, Robert L. and Ellsworth L. Sharpe, A Carbon Dioxide Purge and Thermal Protection System for Liquid Hydrogen Tanks, NASA Conference of Hypersonic Aircraft Technology, Ames Research Center, May, 1967.

MAXWARP, Stephen Corda, University of Maryland, 1989